Article

Molecular Cell

Structural Basis of BRCC36 Function in DNA Repair and Immune Regulation

Graphical Abstract

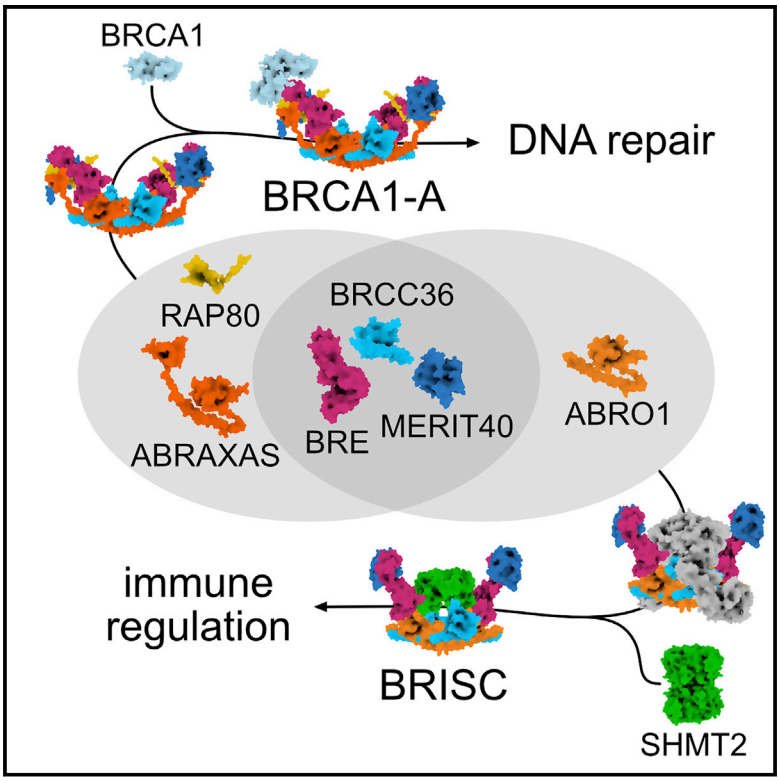

Authors

Julius Rabl, Richard D. Bunker, Andreas D. Schenk, ..., Haico van Attikum, Ronald T. Hay, Nicolas H. Thomä

Correspondence

nicolas.thoma@fmi.ch

In Brief

Structural studies of the BRCA1-A and BRISC complexes reveal a common enzymatic core that is functionalized by complex-specific proteins. BRCA1-A localizes to DNA double-strand breaks, sequesters BRCA1, and suppresses DNA resection. BRISC regulates protein degradation by the endosomal-lysosomal pathway through deubiquitination and is inhibited by the metabolic enzyme SHMT2.

Highlights

- Detailed structural studies of the BRCA1-A and BRISC-SHMT2 protein complex
- Complex-specific subunits functionalize BRCC36, regulating its activity and targeting
- BRCA1-A sequesters BRCA1 with nanomolar affinity
- Cancer-associated metabolic enzyme SHMT2 inhibits BRISC deubiquitination activity

Rabl et al., 2019, Molecular Cell *75*, 483–497
August 8, 2019
https://doi.org/10.1016/j.molcel.2019.06.002

CellPress

Molecular Cell
Article

Structural Basis of BRCC36 Function in DNA Repair and Immune Regulation

Julius Rabl,[1,2,8] Richard D. Bunker,[1,2] Andreas D. Schenk,[1,2] Simone Cavadini,[1,2] Mark E. Gill,[1,2] Wassim Abdulrahman,[1,2,9] Amparo Andrés-Pons,[1,2] Martijn S. Luijsterburg,[3] Adel F.M. Ibrahim,[6] Emma Branigan,[6] Jacob D. Aguirre,[1,2] Aimee H. Marceau,[4] Claire Guérillon,[5] Tewis Bouwmeester,[7] Ulrich Hassiepen,[7] Antoine H.F.M. Peters,[1,2] Martin Renatus,[7] Laurent Gelman,[1,2] Seth M. Rubin,[4] Niels Mailand,[5] Haico van Attikum,[3] Ronald T. Hay,[6] and Nicolas H. Thomä[1,2,10,*]

[1]Friedrich Miescher Institute for Biomedical Research, Maulbeerstrasse 66, 4058 Basel, Switzerland
[2]University of Basel, Petersplatz 10, 4003 Basel, Switzerland
[3]Leiden University Medical Center, Department of Human Genetics, Einthovenweg 20, 2333 ZC Leiden, the Netherlands
[4]Department of Chemistry and Biochemistry, University of California, Santa Cruz, CA, USA
[5]Novo Nordisk Foundation Center for Protein Research, University of Copenhagen, Blegdamsvej 3b, 2200 Copenhagen N, Denmark
[6]Centre for Gene Regulation and Expression, Sir James Black Centre, School of Life Sciences, University of Dundee, Dow Street, Dundee, DD1 5EH, UK
[7]Novartis Institutes for BioMedical Research, Novartis Pharma AG, 4002 Basel, Switzerland
[8]Present address: Scientific Center for Optical and Electron Microscopy (ScopeM), ETH Zürich, 8093 Zürich, Switzerland
[9]Present address: leadXpro AG, PARK innovAARE, 5234 Villigen, Switzerland
[10]Lead Contact
*Correspondence: nicolas.thoma@fmi.ch
https://doi.org/10.1016/j.molcel.2019.06.002

SUMMARY

In mammals, ~100 deubiquitinases act on ~20,000 intracellular ubiquitination sites. Deubiquitinases are commonly regarded as constitutively active, with limited regulatory and targeting capacity. The BRCA1-A and BRISC complexes serve in DNA double-strand break repair and immune signaling and contain the lysine-63 linkage-specific BRCC36 subunit that is functionalized by scaffold subunits ABRAXAS and ABRO1, respectively. The molecular basis underlying BRCA1-A and BRISC function is currently unknown. Here we show that in the BRCA1-A complex structure, ABRAXAS integrates the DNA repair protein RAP80 and provides a high-affinity binding site that sequesters the tumor suppressor BRCA1 away from the break site. In the BRISC structure, ABRO1 binds SHMT2α, a metabolic enzyme enabling cancer growth in hypoxic environments, which we find prevents BRCC36 from binding and cleaving ubiquitin chains. Our work explains modularity in the BRCC36 DUB family, with different adaptor subunits conferring diversified targeting and regulatory functions.

INTRODUCTION

The deubiquitinase (DUB) BRCC36 is the catalytic subunit for two multi-protein complexes: BRCA1-A, which safeguards genome integrity by regulating DNA repair pathway choice, and BRISC, which serves cellular stress response and immune signaling functions (Wu et al., 2012; Yin et al., 2012; Zheng et al., 2013). Both BRCC36-containing complexes are specific for lysine-63-linked ubiquitin (K63-Ub) chains (Cooper et al., 2009; Zeqiraj et al., 2015). BRCA1-A and BRISC also contain proteins MERIT40 (Feng et al., 2009; Shao et al., 2009; Wang et al., 2009) and BRE (Feng et al., 2009; Hu et al., 2011a) as core components. The key compositional differences between the two complexes are the two scaffolding partners of BRCC36 (Figure S1A): in BRCA1-A, BRCC36 is supported by ABRAXAS (Wang et al., 2007), whereas in BRISC, it is paired with ABRO1 (Hu et al., 2011a; Wang et al., 2007). ABRAXAS and ABRO1 are evolutionarily related as they share ~30% identity in humans and contain Mpr1, Pad1 N-terminal (MPN) domains like BRCC36 (Figures S1B and S1C).

BRCA1 and BRCA2 facilitate DNA double-strand break (DSB) repair by homologous recombination (HR), whereas BRCA1-A opposes HR by suppressing resection (Coleman and Greenberg, 2011; Hu et al., 2011b). The BRCA1-A assembly constitutively includes the repair protein RAP80 (Kim et al., 2007; Sobhian et al., 2007; Wang et al., 2007), a protein that recognizes K63-Ub chromatin domains generated by γ-H2AX-dependent DNA damage signaling through RNF4/RNF8/RNF168 (Guzzo et al., 2012; Typas et al., 2015; Uckelmann and Sixma, 2017).

Familial mutations in the BRCA1-A proteins ABRAXAS and RAP80 predispose carriers to early-onset breast cancer, analogous to mutations in *BRCA1* and *BRCA2* (Nikkilä et al., 2009; Solyom et al., 2012). BRCA1-A requires the tandem ubiquitin (UIM_2)- and SUMO-interacting motifs (SIM) in RAP80 and the BRCC36 DUB to function in DNA repair (Guzzo et al., 2012; Hu et al., 2012; Lombardi et al., 2017; Ng et al., 2016). BRCA1-A recruits BRCA1 by binding its BRCT domains upon phosphorylation of a motif near the C terminus of ABRAXAS (Wang et al., 2007). BRCA1 binding to BRCA1-A sequesters the HR activator BRCA1 ~2–10 kb distal from DNA break sites (Goldstein and

Kastan, 2015; Kakarougkas et al., 2013), which is posited to limit HR (Goldstein and Kastan, 2015). It is currently unclear how BRCA1-A is functionalized and targeted by RAP80 and ABRAXAS and how BRCA1 is inhibited when bound to the complex.

While BRCA1-A is predominantly confined to the nucleus, BRISC localizes to the nucleus and the cytoplasm, where its wide range of reported substrates includes ATF4, THAP5, NLRP3, and the cytosolic domain of IFNAR1, an interferon receptor (Ambivero et al., 2012; Cilenti et al., 2011; Py et al., 2013; Zheng et al., 2013). BRISC has been noted to co-purify with serine hydroxy methyltransferase 2 (SHMT2), a metabolic enzyme that converts serine to glycine and a tetrahydrofolate-bound one-carbon unit, and occurs in cytosolic (SHMT2α) and mitochondrial (mSHMT2) forms (Giardina et al., 2015; Sowa et al., 2009; Zheng et al., 2013). SHMT2 is implicated in regulating two medically important aspects of BRISC function, interferon signaling, and viral protein degradation (Xu et al., 2018; Zheng et al., 2013). Since overexpression of SHMT2 plays a pivotal role in the metabolic adaptation of cancer cells to hypoxia (Kim et al., 2015; Lee et al., 2014; Sowa et al., 2009; Zheng et al., 2013), we aimed to understand the functional interplay between BRISC and SHMT2.

While some DUBs have specificity for cleaving distinct ubiquitin-chain linkages, they are not typically regarded as modular, multimeric enzymes and are not assumed to exhibit specificity for individual proteins or pathways. The available data for the BRISC and BRCA1-A complexes, however, suggested that a shared DUB core might assume different roles in DNA repair and immune signaling. To examine the mechanistic circuitry in these multimeric DUB assemblies, we set out to study the molecular basis of BRCA1-A and BRISC regulation and targeting.

RESULTS

Common Architectural Cores of the BRCA1-A and BRISC Assemblies

We determined the structure of the 10-protein mouse BRCA1-A complex (overall molecular weight of 338 kDa; highly similar to human BRCA1-A), comprising two copies each of BRCC36, ABRAXAS, BRE, MERIT40, and RAP80 (residues 274–334) by X-ray crystallography using low-resolution native Zn-SAD phasing methods and carried out final refinement at 3.75 Å resolution (Figures 1A and 1B; Figure S1D; Table 1). In addition, we characterized the structure of the 10-protein human BRISC-SHMT2α complex (overall molecular weight 445 kDa) by cryoelectron microscopy (cryo-EM) at an overall resolution of 3.86 Å (Figures 1B and 1C; Figures S1D, S2A–S2E; Table 2). Analogous to BRCA1-A, the BRISC structure comprises two copies each of proteins BRCC36, ABRO1, BRE, MERIT40, and SHMT2α. We used the A264T mutant of SHMT2α (A285T in mSHMT2) for all structural studies and biochemical characterization, which was originally used to solve the crystal structure of the dimeric apo-SHMT2 (PDB: 6DK3). SHMT2 residue numbers in the text refer to SHMT2α.

In BRCA1-A, two heteropentamers composed of BRCC36, ABRAXAS, BRE, and MERIT40 form an arc-shaped complex with approximate dimensions 213 × 117 × 87 Å^3 (Figure 1A). The two half-arcs contact each other through BRCC36 and its scaffold partner ABRAXAS. While BRCC36 and ABRAXAS both contain MPN domains, only that of BRCC36 is catalytically active (Figure S3A). In our crystals, the BRCC36 catalytic center is captured in an active configuration, with a single catalytic Zn^{2+} ion tetrahedrally coordinated by His122, His124, Asp135, and a water molecule, oriented by Glu33 (Zeqiraj et al., 2015) (Figure S3A). We find that BRCC36 in BRCA1-A and BRISC is activated by assembly due to interaction between Glu30 of BRCC36 and Asn170 in ABRAXAS and Asn164 in ABRO1, respectively, which structures the activation loop and positions the catalytic Glu33 (Figure S3B). This mechanism is homologous to what has been observed in the ancestral BRCC36-KIAA0157 complex (Zeqiraj et al., 2015) but is distinct from that seen in the COP9 signalosome (CSN) and the proteasome lid, where the position of the scaffold MPN domain differs (Figure S3B) (Lingaraju et al., 2014; Pathare et al., 2014; Worden et al., 2014, 2017).

In the BRCA1-A complex structure, the ABRAXAS MPN domain plays a key structural role connecting the catalytically active BRCC36 subunit to the distal part of the arc consisting of BRE, MERIT40, and RAP80 (Figure 1A). BRE, in turn, forms the central bridge between the ABRAXAS-BRCC36 MPN domain dimer and the Von-Willebrand factor A (VWA) domain protein MERIT40 (Figures 1A and 2A). BRE contains N- and C-terminal ubiquitin E2 variant (UEV) domains (Figure 2A). We identify a new, third domain in BRE, a previously unidentified central RING-finger containing, WD-repeat-containing proteins and yeast DEAD (DEXD)-like helicase domain (RWD) located between the UEV domains (Figures 1B and 2A; Figure S3C). The BRE RWD and C-terminal UEV (UEV-C) domains are connected by a continuous helix, similar to the arrangement of the UEV and RWD domain observed in human DNA repair protein FANCL (Hodson et al., 2011) (Figure S3D). The BRE N-terminal UEV domain (UEV-N) binds the ABRAXAS MPN domain, and the BRE UEV-C holds MERIT40 at the extremity of the arc (Figure 2A).

In the BRCA1-A complex, the two heteropentamers are intimately linked by a bundle of four αhelices comprising the C-terminal tails of BRCC36 and ABRAXAS (Figure 1A; Figure S3E). An ABRAXAS linker segment and an α helix crossover from one site of the half-arc to the other effectively interlock the two pentamers (Figure S3E). The same arrangement is found in BRISC (Figure S3E). This crossover arrangement is not observed in the ancestral BRCC36/KIAA0157 subcomplex (Figure S3E), where dissociation of the two pentamers has been suggested as a putative mechanism to regulate activity (Zeqiraj et al., 2015). Given the observed pseudo-knotted arrangement, regulation by dissociation is unlikely in the case of mammalian BRCA1-A, and instead, we find that accessory subunits, such as RAP80, have appeared in the evolutionary lineage to confer targeting and regulatory capabilities.

The BRCA1-A/BRISC Architecture Offers a Scaffold for Ubiquitin Binding

In light of the multiple ubiquitin-binding modules in BRE, we tested BRCA1-A with K63-linked chains of different length ranging from di-ubiquitin $(Ub)_2$ and tri-ubiquitin $(Ub)_3$ to tetra-ubiquitin $(Ub)_4$. BRE contains UEV/RWD binding domains, with a K63-linked ubiquitin-binding site previously reported for the BRE-MERIT40 complex (Kyrieleis et al., 2016). We saw preferential cleavage of

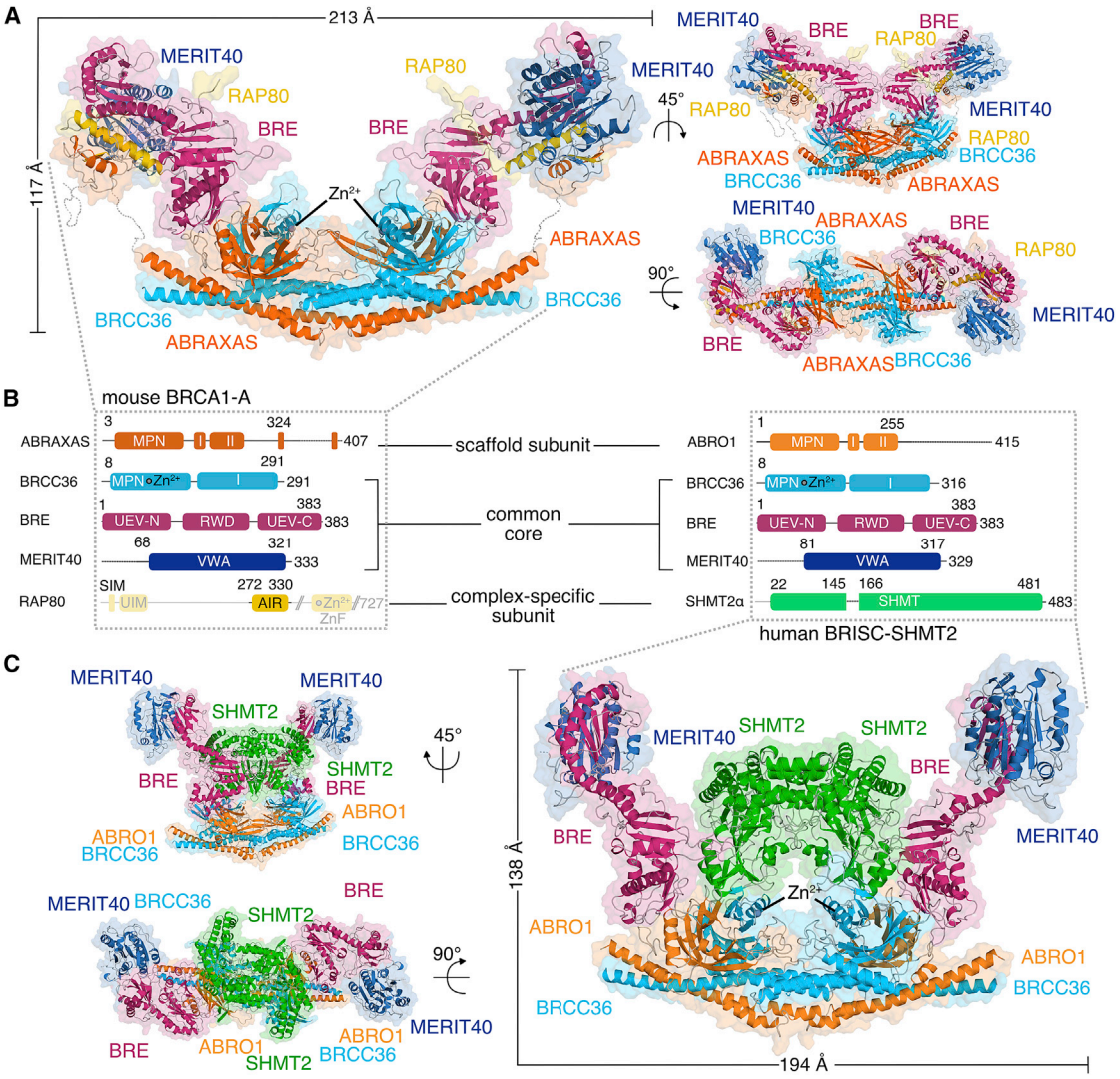

Figure 1. Structures of the BRCA1-A and BRISC-SHMT2α Complexes

(A) A cartoon representation of the BRCA1-A complex crystal structure.

(B) Schematic representation of the domain boundaries of BRCA1-A and BRISC-SHMT2α, showing parts present in the structure (domain cartoons and solid line), parts that are present in the construct but disordered in the structure (dashed line), and parts not present in the construct (grayed out domain cartoons and solid gray line).

(C) A cartoon representation of the BRISC-SHMT2α complex cryo-EM structure.

$(Ub)_4$, while no cleavage of $(Ub)_2$ and $(Ub)_3$ chains was observed under these conditions (Figure 2B). BRISC similarly exhibited preferential cleavage for longer chains (Figure S3F). Cleavage of $(Ub)_2$, however, was seen when reactions were run at higher temperatures and enzyme concentrations (Figure S3G). $(Ub)_4$ units span ~90 Å and may thus connect the BRCC36 active site to BRE and potentially MERIT40. In light of the structure, we tested whether the VWA domain of the distal MERIT40 itself also potentially contributed to ubiquitin binding. NMR binding studies using ^{15}N-labeled ubiquitin found mono-ubiquitin binding to BRE-MERIT40 complex with estimated micromolar affinity (Figure S3H). Additionally, the isolated MERIT40 subunit bound ubiquitin with estimated high micromolar affinity (Figure S3H), comparable to established ubiquitin-binding domains (Hicke et al., 2005). The arc-shaped BRCA1-A/BRISC architecture thus offers a ubiquitin-binding scaffold potentially ranging from the BRCC36 active site located at the middle of the arc up to the MERIT40 subunits located at the tip.

We then tested whether this arrangement pre-orientates the $(Ub)_4$ chains for cleavage or whether the ubiquitin-binding modules predominately serve to generate high local concentrations. For this, we introduced fluorescent labels on either the proximal or the distal end of $(Ub)_4$ chains (Figure 2C). Incubating the proximally labeled substrate with BRCA1-A, we mostly observed $(Ub)_2$ and $(Ub)_3$ cleavage products, while the distally labeled sample resulted in a different cutting pattern, accumulating

Table 1. BRCA1-A Crystallographic Data Collection and Refinement Statistics

	Native Zn-SAD	PDB: 6GVW[a]
Data Collection		
Space group	$P2_12_12_1$	$P2_12_12_1$
Cell dimensions		
a, *b*, *c* (Å)	97.07, 122.71, 431.94	97.10, 112.64, 431.33
Resolution (Å)	118–4.30 (4.374–4.300)[b]	30–3.75 (3.814–3.750)
R_{meas}	0.217 (>3.000)	0.175 (>3.000)
R_{pim}	0.024 (1.814)	0.025 (2.173)
$CC_{1/2}$	0.999 (0.305)	0.952 (0.476)
Mean $I/\sigma I$	18.3 (0.5)	11.6 (0.4)
Multiplicity	79.6 (79.1)	51.9 (52.8)
Completeness (%)		
Spherical	100 (100)	100 (100)
Ellipsoidal	–	82.6 (33.2)[c]
Refinement		
Resolution (Å)	–	30–3.75
No. reflections	–	42,193
R_{work}/R_{free} (%)	–	22.72/25.91
No. atoms		
Protein	–	20,138
Zn^{2+} ions	–	2
Water	–	2
B factors		
Protein	–	229
Zn^{2+} ions	–	193
Water	–	163
RMSDs		
Bond lengths (Å)	–	0.006
Bond angles (°)	–	1.147

[a]Data from 7 crystals were combined
[b]Values in parentheses are for highest-resolution shell
[c]After anisotropic truncation with *STARANISO* as used for refinement

Table 2. Cryo-EM Data Collection, Refinement, and Validation Statistics

	BRISC-SHMT2 (EMDB: EMDB-0132; PDB: 6H3C)
Data Collection and Processing	
Magnification	58,140
Voltage (kV)	300
Electron exposure ($e^-/Å^2$)	45
Defocus range (μm)	−0.5 to −5
Pixel size (Å)	0.86
Symmetry imposed	C2
Initial particle images (no.)	332,598
Final particle images (no.)	35,595
Map resolution (Å)	3.86
FSC threshold	0.143
Map resolution range (Å)	3.86–15
Refinement	
Initial model used (PDB code)	BRCA1-A (PDB: 6GVW), SHMT2 (PDB: 5V7I)
Model resolution (Å)	3.86
FSC threshold	0.143
Map sharpening *B* factor ($Å^2$)	N/A
Model composition	
Non-hydrogen atoms	25,134
Protein residues	3,154
Water	2
B factors ($Å^2$)	
Protein	90.25
Water	64.48
RMSDs	
Bond lengths (Å)	0.020
Bond angles (°)	1.93
Validation	
MolProbity score	1.32
Clashscore	1.88
Poor rotamers (%)	0.07
Ramachandran plot	
Favored (%)	94.56
Allowed (%)	4.8
Disallowed (%)	0.64

predominantly Ub cleavage products (Figure 2C). These findings are consistent with alignment of the $(Ub)_4$ chain with the distal ubiquitin, pointing toward BRCC36, being cleaved first, in a process likely supported by the multiple ubiquitin-binding domains on BRE and MERIT40.

BRCA1-A RAP80 Integration

BRCA1-A activity in DNA repair critically depends on the presence of RAP80. Our crystal structure now demonstrates how the RAP80 subunit functionalizes the complex. We find that the RAP80 protein is solubilized and stabilized by the presence of BRCA1-A and stably maintained in all purification steps. Our BRCA1-A structure reveals that RAP80 is deeply integrated into the BRCA1-A assembly by interactions with three subunits: ABRAXAS, BRE, and MERIT40 (Figures 1A and 2A). The N-terminal portion (Gly272-Trp278) of the RAP80 ABRAXAS-interacting region (AIR) engages MERIT40, the trailing α helix (Asn290-Leu314) binds across the BRE UEV-C domain, with the RAP80 C terminus forming a β strand (Val315-Phe330) sandwiched by the RWD and UEV-N domains of BRE. The ABRAXAS C terminus binds the α helix of RAP80 AIR through an α-helical domain (Ile277-Phe287), and the RAP80 AIR β sheet stacks in-between β sheets from MERIT40 and ABRAXAS (Figure 2A). The structural elements of RAP80 AIR are highly conserved (Figure S4A).

While the region in RAP80 that mediates BRCA1-A binding is short, it is essential for BRCA1-A function (Figures S4B–S4D). It also gives rise to a relatively large interface between RAP80

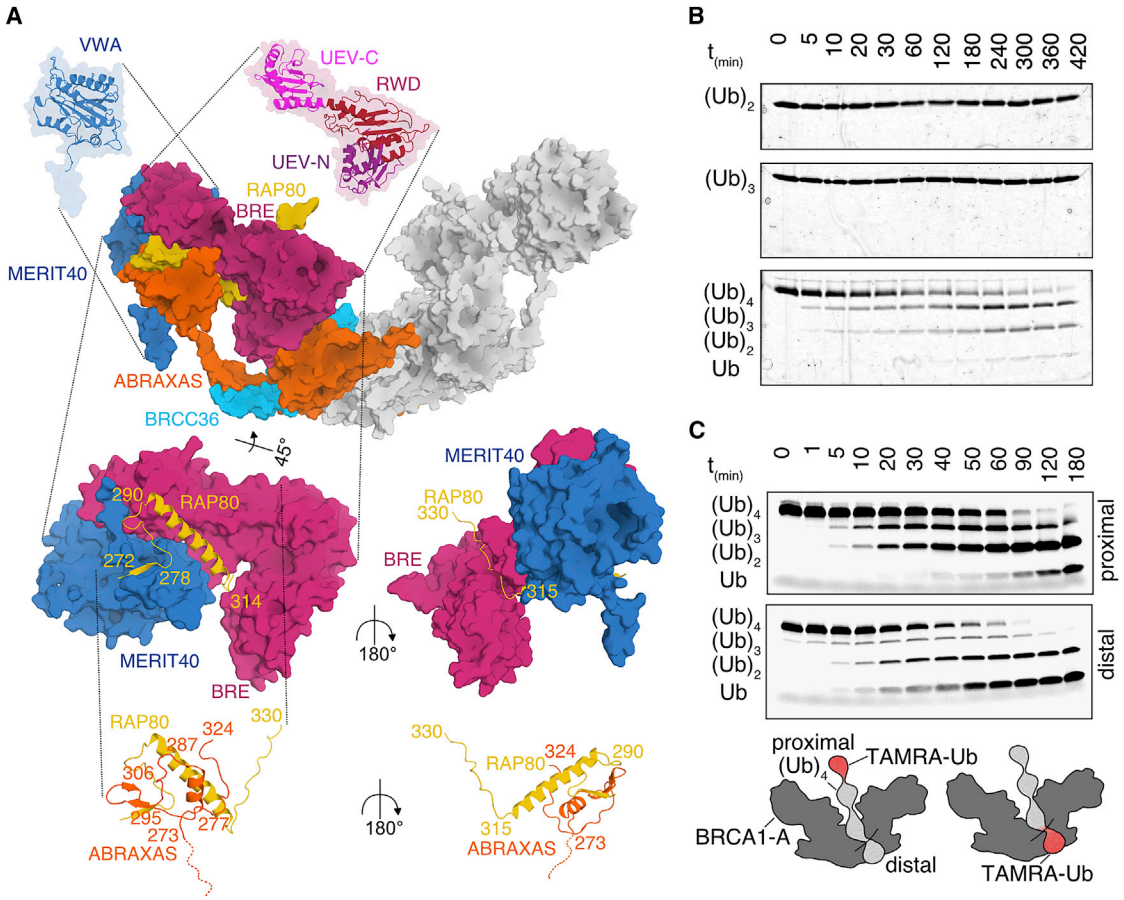

Figure 2. Integration of RAP80 and DUB Specificity of BRCA1-A

(A) The position of the UEV-N, RWD, and UEV-C domains of BRE and the VWA domain of MERIT40 (shown as cartoon) within the BRCA1-A complex (shown as surface). RAP80 is embedded into the complex through contacts with BRE, MERIT40, and ABRAXAS.

(B) BRCA1-A complex processes $(Ub)_4$ faster than $(Ub)_3$ and $(Ub)_2$. K63-linked ubiquitin substrate (150 ng/lane) was incubated with 5 nM BRCA1-A on ice and analyzed by silver-stained SDS-PAGE. Under these conditions, $(Ub)_4$ is cleaved within 5 min, whereas $(Ub)_2$ and $(Ub)_3$ are not cleaved within 7 h.

(C) Tetra-ubiquitin chains are pre-oriented on BRCA1-A complex during cleavage, as evident from comparison of the degradation of K63-linked $(Ub)_4$ substrate labeled with TAMRA at the proximal and distal ubiquitin, respectively. Degradation products of 1 μM substrate incubated with 10 nM BRCA1-A at room temperature were resolved on an SDS-PAGE; TAMRA was subsequently visualized.

and BRE (1,951 Å^2 buried surface area) and MERIT40 (822 Å^2). It is the interaction with ABRAXAS (1,146 Å^2), however, that drives specific incorporation of RAP80 into BRCA1-A: while BRISC alone integrates co-expressed RAP80 substoichiometrically (Figure S4E), a hybrid BRISC complex that contains a fusion scaffold protein, in which the C-terminal tail of ABRO1 (261–415) is exchanged for that of ABRAXAS (269–407), tightly integrates RAP80 (Figure 3A). The BRCA1-A-specific ABRAXAS subunit drives RAP80 integration, while the BRE/MERIT40 subunits present in both BRISC/BRCA1-A complexes play an important accessory role. Since BRISC and RAP80 are targeted to different cellular compartments, association between BRISC and RAP80 is not observed *in vivo* despite the presence of BRE and MERIT40 (Feng et al., 2010).

Our structure of BRCA1-A explains the observation that loss of BRE, or MERIT40, significantly impairs BRCA1-A function, resulting in DNA repair defects and loss of cancer suppression similar to what was seen for loss of RAP80 (Feng et al., 2009; Hu et al., 2011a; Patterson-Fortin et al., 2010; Rebbeck et al., 2011; Shao et al., 2009). The high degree of structural interdependence between RAP80, BRE, and MERIT40 means that the physical link between RAP80 and ABRAXAS, which is essential for DNA repair, can no longer be efficiently retained in BRCA1-A once BRE (accounts for ~50% of the RAP80 interface) or MERIT40 (accounts for ~20%) is lost.

RAP80 binding further affects the BRCA1-A quaternary structure. A previous ~20 Å low-resolution structure of truncated BRCA1-A determined in the absence of RAP80 and using chemical crosslinking reported the dimerization of two full BRCA1-A arcs (Kyrieleis et al., 2016). We find that BRISC in the absence of SHMT2 exists in an equilibrium between single arc and dimer, which can be shifted toward the dimer by chemical crosslinking, analogous to truncated BRCA1-A without RAP80 (Figures 3A and 3B; Figures S4F and S4G). We observe a single arc of

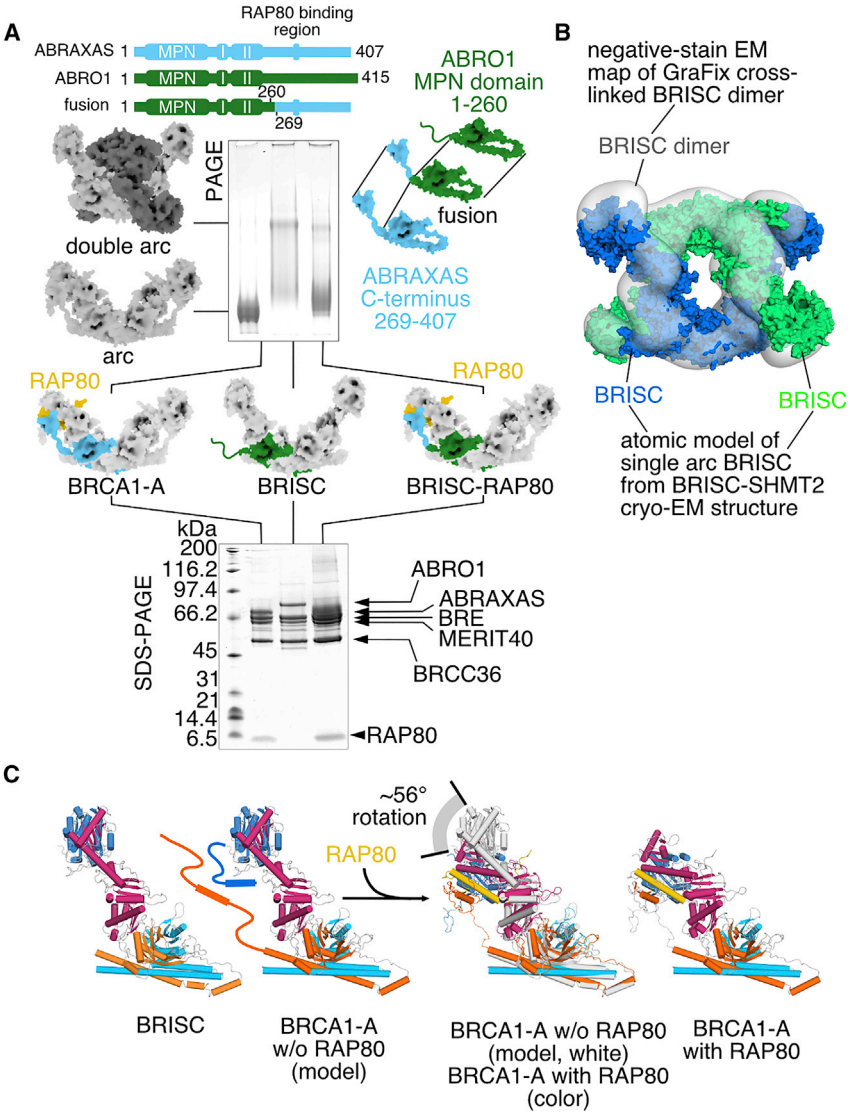

Figure 3. RAP80 Controls BRE Conformation and Prevents Dimerization

(A) A fusion scaffold protein containing residues 1–260 of mouse ABRO1 fused to residues 269–407 of mouse ABRAXAS disrupts dimerization (native PAGE) and integrates RAP80 stoichiometrically into the complex (SDS-PAGE).

(B) The structure of BRISC dimer. A pseudoatomic model of BRISC was generated by rigid-body fitting of the atomic BRISC model derived from the cryo-EM structure determination of BRISC-SHMT2α complex into the density map of BRISC dimer.

(C) Integration of RAP80 into BRCA1-A results in a substantial conformation change of BRE as evidenced by a comparison of the structures of BRCA1-A and BRISC.

RAP80-bound BRCA1-A in our crystal structure (Figure 1A) and in negative-stain EM studies, irrespective of the use of chemical crosslinking (Figure S4H). The presence of RAP80 binding results in a structural change in BRE and MERIT40, which in turn prevents dimerization of the two arcs (Figure 3C; Figure S4I). RAP80 is essential for BRCA1-A complex assembly and stability *in vivo* (Bian et al., 2012), and its cellular concentration exceeds that of ABRAXAS (Mok and Henderson, 2012). This, together with the observed intricate structural integration of RAP80 into BRCA1-A, suggests that RAP80 is a constitutive member of the BRCA1-A complex and that the single arc observed in our structure likely depicts the physiological assembly.

SUMO-Dependent Targeting of BRCA1-A

The RAP80 N-terminal region contains SIM (residues 41–43) and K63-linkage- specific tandem UIM domains (residues 80–99 and 105–124) that bind mixed ubiquitin-SUMO chains with high affinity (Guzzo et al., 2012; Hu et al., 2012). These domains recruit BRCA1-A to sites of DNA damage (Guzzo et al., 2012; Hu et al., 2012) and are connected to BRCA1-A via a flexible linker (Figure S4J).

We thus tested whether the RAP80 SIM/UIM units serve in recruitment only or whether they also contribute to preferential cleavage of mixed SUMO ubiquitin chains. For this, we monitored degradation of $(Ub)_2$ and SUMO/di-ubiquitin (SUMO-K63-diUb) chains by BRCA1-A in gel-based cleavage assays (Figure S5A). We found a small preference in cleavage of SUMO-K63-Ub_2 chains in the presence of full-length RAP80, but not with BRCA1-A variants that lack the RAP80 SIM-UIM_2 (Figure S5B). In light of the preferential cleavages of $(Ub)_4$ over $(Ub)_2$ chains, we then switched to longer SUMO-K63 chains with, on average, more than 6 ubiquitin units. In the context of these longer chains, the RAP80 SIM/UIM module did not confer a robust effect on cleavage (Figure S5C). This result suggests that the role of the RAP80 SIM/UIM module lies predominantly in recruiting the complex to sites of SUMO and ubiquitin modifications.

BRCA1 Sequestration by BRCA1-A Complex

A key BRCA1-A function is to regulate BRCA1 activity in DSB repair. BRCA1-A and BRCA1 form a complex that sequesters BRCA1 distant from the site of damage, an important regulatory step in HR (Goldstein and Kastan, 2015; Kakarougkas et al., 2013). This is dependent on the presence of RAP80, and a correctly assembled BRCA1-A complex, but does not require BRCC36 DUB activity (Ng et al., 2016). The ABRAXAS C terminus phosphorylated at Ser406 binds the BRCA1-BRCT 1 (residues 1,642–1,736) and BRCT 2 (residues 1,756–1,855) domains (BRCA1-BRCT) with an apparent K_d of ~1.2 μM, an affinity comparable to that of other BRCA1-BRCT interaction partners (Badgujar et al., 2013; Wu et al., 2016). Given comparable affinities with other BRCA1-BRCT binders, it was unclear how

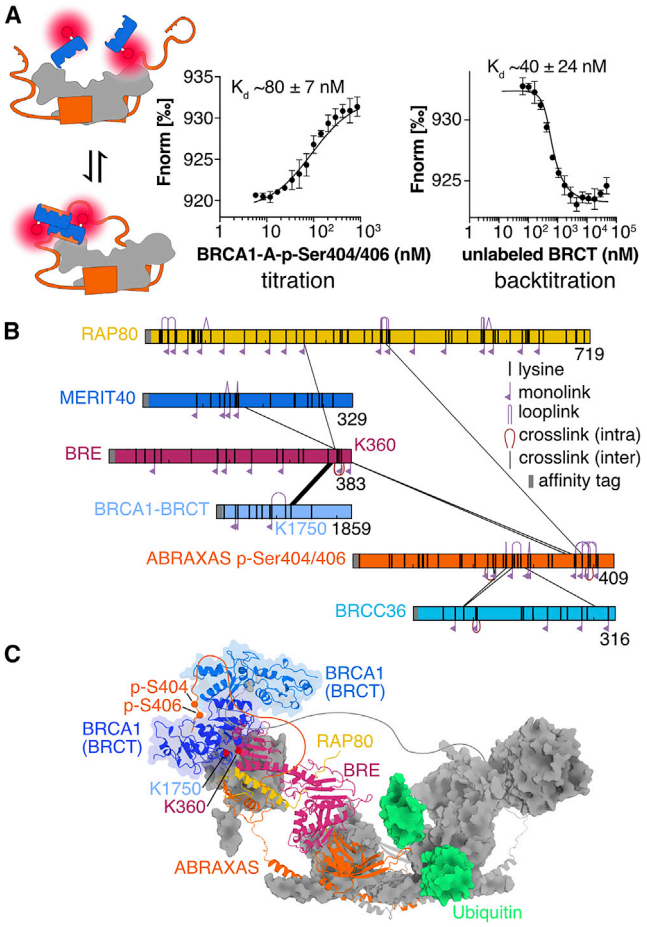

Figure 4. BRCA1-A Forms a Defined High-Affinity Complex with BRCA1

(A) In an MST assay measuring binding of labeled BRCA1-BRCT to full-length BRCA1-A complex including phosphorylated p-Ser404/406 ABRAXAS C terminus, BRCA1-BRCT is bound with nanomolar affinity. The assay measures change of relative fluorescence during heating; values are $F_{norm} = F_{hot} / F_{cold}$. Error bars represent mean ± SD of n = 4 replicates. Back titration with unlabeled BRCA1-BRCT confirms nanomolar affinity. Error bars represent mean ± SD of n = 4 replicates.

(B) Crosslinking network of the BRCA1-A-BRCA1 complex. Proteins are shown schematically as bars. Crosslinks are shown as black lines. The crosslink between K360 of BRE and K1750 of BRCA1 is conditional on the presence of p-Ser404/406 phosphorylation on ABRAXAS C terminus.

(C) Model of the BRCA1-A-BRCA1 high-affinity complex. One protomer of ABRAXAS, BRE, and RAP80 is shown as cartoon, while the remainder of the BRCA1-A complex is shown as gray surface. A BRCA1-BRCT dimer (blue, cartoon) is depicted in a position that localizes K1750 of BRCA1 proximal to K360 of BRE. The unstructured C-terminal regions of ABRAXAS are depicted schematically as orange and gray lines. A di-ubiquitin (green, surface) is shown modeled into the active site.

BRCA1-A, an inhibitor of resection, can potentially sequester BRCA1 away from other binding partners such as BACH1 or CtIP that typically activate HR (Badgujar et al., 2013; Clapperton et al., 2004; Shiozaki et al., 2004; Varma et al., 2005; Wu et al., 2016).

We set out to quantify BRCA1 binding to BRCA1-A in the context of the fully assembled complex. Activation of the DSB repair checkpoint has been suggested to proceed via the double-phosphorylated ABRAXAS variant p-Ser404/406 in conjunction with induced dimerization of the BRCA1-BRCT (Wu et al., 2016). We generated the entire BRCA1-A complex with site-specifically phosphorylated ABRAXAS by ligating phosphorylated C-terminal peptides by sortase-mediated transpeptidation (Figures S5D and S5E). In microscale thermophoresis (MST) experiments, measuring binding of labeled BRCA1-BRCT domains to the entire BRCA1-A complex bearing ABRAXAS p-Ser404/406, we observed substantially higher affinity (K_d ~80 ± 7 nM) (Figure 4A) than what is typically reported for BRCA1-BRCT domain binding. The doubly phosphorylated ABRAXAS p-Ser404/406 integrated in the BRCA1-A complex thus provides a high-affinity docking cradle for BRCA1, exceeding the affinity of other known BRCA1 interactors by more than 10-fold (Badgujar et al., 2013; Liu and Ladias, 2013; Ray et al., 2006; Shiozaki et al., 2004; Varma et al., 2005).

The increased interaction between BRCA1 and the BRCA1-A complex likely arises from increased avidity due to the dimeric structure of the BRCA1-A arc but also potentially suggests further contacts extending beyond the BRCA1-BRCT ABRAXAS phosphopeptide interface. We compared the interaction between BRCA1-BRCT and non-modified or p-Ser404/406 phosphorylated BRCA1-A in a crosslinking mass spectrometry experiment and observed a specific crosslink between BRCA1-A subunit BRE (Lys360) and BRCT (Lys1750) that was dependent on the presence of p-Ser404/406 modifications in ABRAXAS (Figure 4B). The unstructured linker in ABRAXAS that separates the RAP80-binding domain from the phosphorylated BRCA1-binding motif allows the BRCA1-BRCT dimer to reach BRE (UEV-C) at either side of the arc (Figure 4C).

We have not observed higher-order assemblies of multiple BRCA1-A arcs stabilized by BRCA1-BRCT in negative-stain EM (data not shown) or mobility shift assays (Figure S5E) that had previously been proposed (Kyrieleis et al., 2016). We also did not detect a difference in activity when assaying the phosphorylated BRCA1-A complex in the presence or absence of the BRCA1-BRCT (Figure S5F).

Our data instead support a model where ABRAXAS integrates RAP80 specifically into BRCA1-A, thereby preferentially targeting the BRCC36 DUB to DNA repair foci with both SUMO and K63-Ub chains. Following checkpoint activation, the phosphorylated ABRAXAS subunit in BRCA1-A provides the high-affinity binding site for BRCA1 sequestration and inhibition away from the break site.

BRISC-SHMT2α Architecture

BRISC and BRCA1-A are functionalized by the ABRO1 and ABRAXAS subunits, respectively, that work together with dedicated adaptor proteins. The BRISC core (BRCC36-ABRO1 MPN dimer, UEV-N and RWD domain of BRE) has the same 2-fold symmetrical arc shape and is structurally similar to BRCA1-A (RMSD 2.8 Å). The conformation of BRE UEV-C and MERIT40, however, differs markedly, with MERIT40 in BRISC rotated by ~56° in respect to its position in the BRCA1-A crystal structure. We found the structural change to be induced by RAP80 binding to BRCA1-A (Figures 1A, 1C, 3A, and 3C). Whereas RAP80 is constitutively integrated into BRCA1-A,

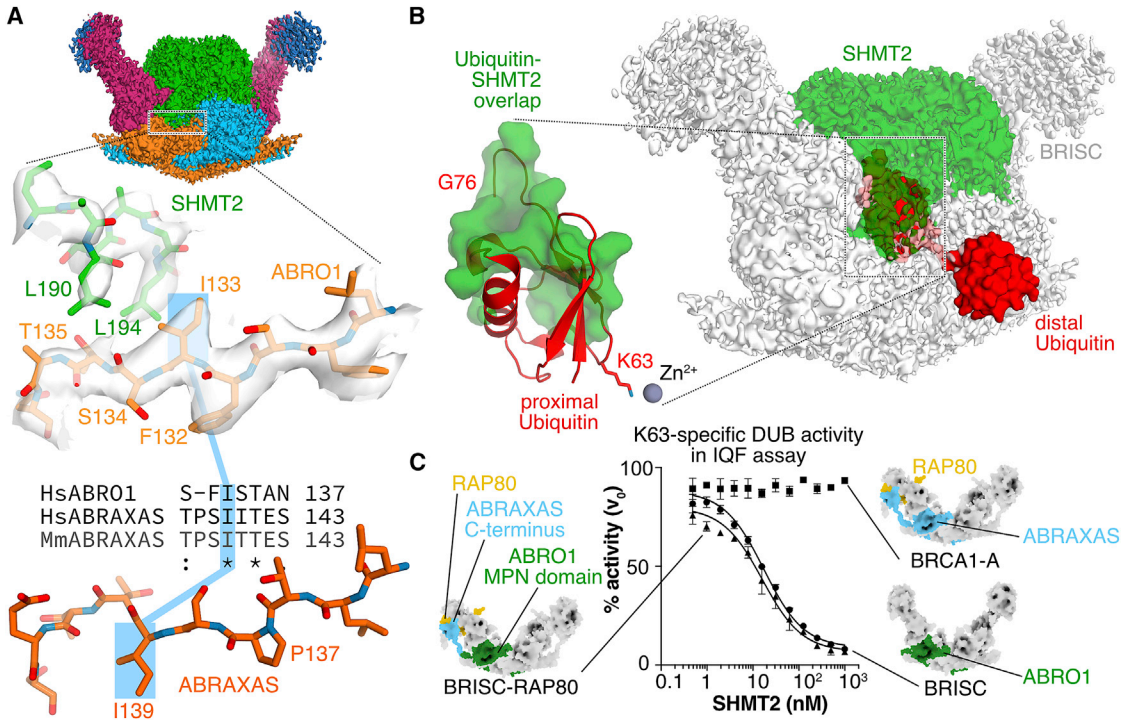

Figure 5. Metabolic Enzyme SHMT2α Binds Specifically to BRISC, Inactivating It

(A) The cryo-EM structure of BRISC-SHMT2α reveals why SHMT2α binds BRISC, but not BRCA1-A. While the ABRO1 isoleucine (Ile133) proximal to SHMT2α is conserved in ABRAXAS, it points away from SHMT2α due to insertion of a proline (Pro137) into ABRAXAS.

(B) SHMT2 clashes with the position of the proximal ubiquitin of a ubiquitin dimer bound to the active site. Modeling di-ubiquitin (red, surface) into the BRCC36 active site reveals a substantial clash with the position of SHMT2α (green) in the BRISC-SHMT2α map (semitransparent surface).

(C) SHMT2α is a potent inhibitor of BRISC (2 nM), but not of BRCA1-A (5 nM), as shown by SHMT2α-mediated inactivation of BRISC in a DUB-activity assay using IQF K63-linked di-Ubiquitin. A BRISC-RAP80 fusion construct (2 nM) containing the MPN domain of ABRO1 combined with the C terminus of ABRAXAS integrates RAP80 like BRCA1-A but is inhibited by SHMT2α like BRISC. Error bars represent mean ± SD of n = 3 replicates.

SHMT2 has an established BRISC-independent role in one-carbon metabolism (Giardina et al., 2015; Kim et al., 2015). SHMT2 is expressed in a mitochondrial and a cytosolic form (SHMT2α) (Anderson and Stover, 2009). SHMT2α is the form encountered by BRISC *in vivo*, because BRISC does not enter mitochondria. BRISC in isolation is present in a two-arc assembly (Figures 3A and 3B; Figures S4F, S4G, and S4I) not suitable for high-resolution structure determination due to structural heterogeneity. SHMT2α binding converts BRISC into a single-arc arrangement (Figure 1C). The BRISC-SHMT2 complex is recruited to the K63-modified IFNAR1 receptor and has been implicated in IFNAR1 deubiquitination (Zheng et al., 2013). Furthermore, BRISC-SHMT2 controls viral Tat protein degradation in HIV-1-infected cells (Xu et al., 2018). The BRISC-SHMT2α structure now illustrates how ABRO1 allows SHMT2α binding to BRISC and how SHMT2α functionalizes the complex beyond what is expected from an adaptor.

The BRISC-bound SHMT2α is catalytically inactive (Zheng et al., 2013), which is explained by our structure. Active SHMT2α when bound to its pyridoxal-5′-phosphate (PLP) cofactor is a tetramer (Giardina et al., 2015). In the absence of its cofactor, mammalian SHMT2 forms a structurally "open" apo-SHMT2 dimer that is enzymatically inactive (Giardina et al., 2015). SHMT2α bound to the center of the BRISC arc is present as a dimer, and each protomer forms an extended 1,161 Å^2 interface involving subunits ABRO1, BRCC36, and BRE in BRISC (Figure 1C; Figure S5G). In complex with BRISC, the SHMT2α dimer adopts the open conformation, the structural hallmarks of the inactive PLP cofactor-free enzyme (Figures S5H and S5I).

Two key hydrophobic SHMT2α residues, Leu190 and Leu194, pack against ABRO1 residues Ile133, Ser134, and Thr135 (Figure 5A). An extended loop in SHMT2α (residues Gly274-Tyr288) contacts BRE residues Lys162-Ala167, and Phe195 of SHMT2α interacts with Trp130 of BRCC36 (Figures S5J and S5K). Mutation of the ABRO1-interacting SHMT2α residues Leu190 and Leu194 to lysine reduced BRISC binding in bio-layer interferometry by more than 10-fold (SHMT2α binding to BRISC: apo K_d ~46 nM, PLP-preincubated K_d ~39 nM; SHMT2α Leu190Lys, Leu194Lys: K_d ~530 nM) (Figure S6A). Analogous to what we saw for RAP80/ABRAXAS in BRAC1-A, it is the BRISC-specific ABRO1 subunit, with help of the remainder of the complex, that is required for SHMT2α integration.

SHMT2α Functions as a BRISC Inhibitor

A model of K63-linked di-ubiquitin chains on BRCC36 using AMSH-LP as a template (Sato et al., 2008) finds SHMT2α potentially blocking substrate access to the active site (Figure 5B). We therefore tested whether BRISC is inhibited when in complex

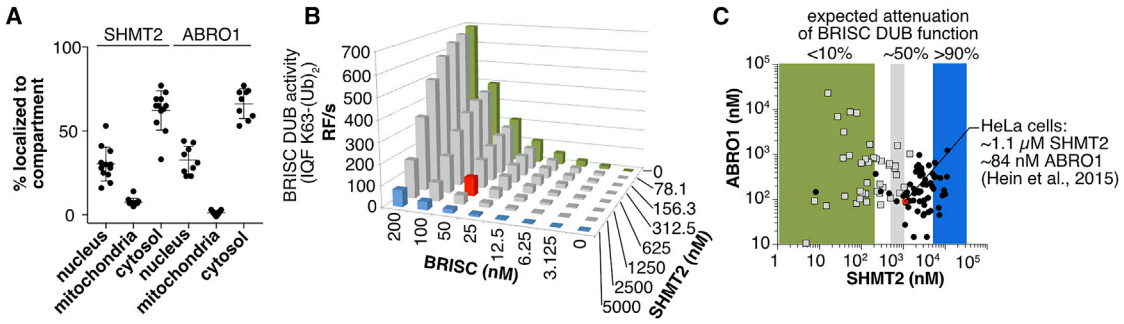

Figure 6. BRISC and SHMT2 Share the Same Cellular Compartments *In Vivo* and Vary in Concentration across Cell Lines and Tissues

(A) Endogenous SHMT2 and ABRO1 colocalize to nucleus and cytosol in quantitative immunofluorescence experiments. Error bars represent mean ± SD. SHMT2: n = 13 replicates. ABRO1: n = 9 replicates. Every image contained 2–10 individual cells.

(B) BRISC DUB activity at substrate and SHMT2 concentrations encountered inside healthy and diseased human cells ranges from fully active to completely inhibited. BRISC DUB activity corresponding to the concentrations of SHMT2α and ABRO1 in HeLa cells is shown in red.

(C) Concentrations of ABRO1 and endogenous SHMT2 in healthy human tissues (gray squares) and cancer cell lines (black circles) suggest that BRISC is attenuated by no more than 50% in healthy human cells but mostly inhibited in cancer cell lines. Concentrations of SHMT2 and ABRO1 corresponding to HeLa cells are shown in red.

with SHMT2α. For this, we monitored the cleavage of K63-linked $(Ub)_2$ substrates by BRISC in the presence of SHMT2α. In fluorescent di-ubiquitin cleavage assays, SHMT2α inhibited K63-linked $(Ub)_2$ cleavage by BRISC in a concentration-dependent manner, with an estimated apparent K_i ~7 ± 0.3 nM, which is comparable to the binding constant between SHMT2α and BRISC determined by bio-layer interferometry (K_d ~39 nM) (Figures S6A and S6B). Mutating SHMT2α residues Leu190 and Leu194 required for ABRO1 binding to Lys190 and Lys194 abolished BRISC inhibition by SHMT2α (Figure S6C). In addition to a possible role of SHMT2α in targeting BRISC to membranes, SHMT2α serves as a soluble DUB inhibitor when engaged. We find that the inhibitory effect of SHMT2α on BRISC is not affected by concentrations of PLP, serine, glycine, or tetrahydrofolate tested (Figures S6D–S6G).

We then tested whether SHMT2α inhibition was specific to BRISC and examined which epitopes of ABRO1 are involved. Unlike BRISC, BRCA1-A was not inhibited by SHMT2α, but a chimeric BRCA1-A complex bearing the MPN domain of ABRO1 (1-260) instead of ABRAXAS (1-269) was inhibited by SHMT2α (Figure 5C). Although in BRISC the SHMT2α-binding interface consists of BRE, ABRO1, and BRCC36, it is primarily the BRISC-specific subunit ABRO1, this time through its MPN domain, that confers specific SHMT2α binding. While ABRAXAS contains the equivalent of the SHMT2α-binding ABRO1 Ile133 residue (Ile139), an adjacent deletion of one residue flips the isoleucine side chain away from the interface, providing the structural basis of specificity (Figure 5A). SHMT2α thus functions as a specific, high-affinity protein inhibitor of the BRISC MPN DUB complex by restricting access to the active site, and this property is specifically conferred by ABRO1. Since BRCA1-A does not bind SHMT2α, BRCA1-A activity in DNA repair signaling is unaffected by nuclear SHMT2α.

SHMT2α as a Cell-Type-Dependent Regulator of BRISC Activity

The observed high-affinity binding and potent mutual inhibition between BRISC and SHMT2α *in vitro* led us to examine whether the concentration of BRISC-SHMT2α and its subcellular distribution would permit regulation *in vivo*. Pre-processed SHMT2 and a mature form cleaved after residue Ser29 predominantly localized to the mitochondria in mouse liver cells (Anderson and Stover, 2009). SHMT2α, however, is found in comparable amounts in the nucleus, cytosol, and mitochondria (Anderson and Stover, 2009). All SHMT2 isoforms are expected to inhibit BRISC based on our structure. To determine BRISC and total SHMT2 subcellular localization, we carried out immunofluorescence experiments using a SHMT2 antibody for an epitope common to all three forms of SHMT2 (Figure S6H). We found endogenous SHMT2 in HEK293 cells present in the cytosol (62.1% ± 11.7%), nucleus (30.3% ± 10.0%), and mitochondria (7.6% ± 2.2%). The BRISC-specific subunit ABRO1 was found in the cytosol (66.2% ± 8.8%) and in the nucleus (32.6% ± 8.2%) but was not detected in mitochondria (Figure 6A). Using quantitative mass spectrometry, concentrations on the order of ~1 μM SHMT2 and ~20–100 nM BRISC were measured in HeLa cells (Hein et al., 2015). To determine the expected extent of BRISC inhibition by SHMT2, we carried out *in vitro* internally quenched fluorescent (IQF) di-ubiquitin cleavage assays. At concentrations of BRISC and SHMT2α found in HeLa cells, BRISC DUB activity is expected to be inhibited by SHMT2 up to 50% (Figure 6B). In cancer cell lines surveyed by quantitative mass spectrometry, endogenous SHMT2 is present in concentrations exceeding 1 μM (Hein et al., 2015; Wilhelm et al., 2014), which corresponds to BRISC inhibition of more than 80% in our assays (Figure 6C). Across a variety of cell lines and tissues, SHMT2 and BRISC therefore are present at concentrations that permit BRISC inhibition, allowing SHMT2 to potentially regulate BRISC-mediated K63 deubiquitination activity.

DISCUSSION

Our results demonstrate how a near identical deubiquitinase core is functionalized for radically different cellular purposes through the ABRO1 and ABRAXAS subunits and how these subunits confer differential BRCC36 targeting and regulation.

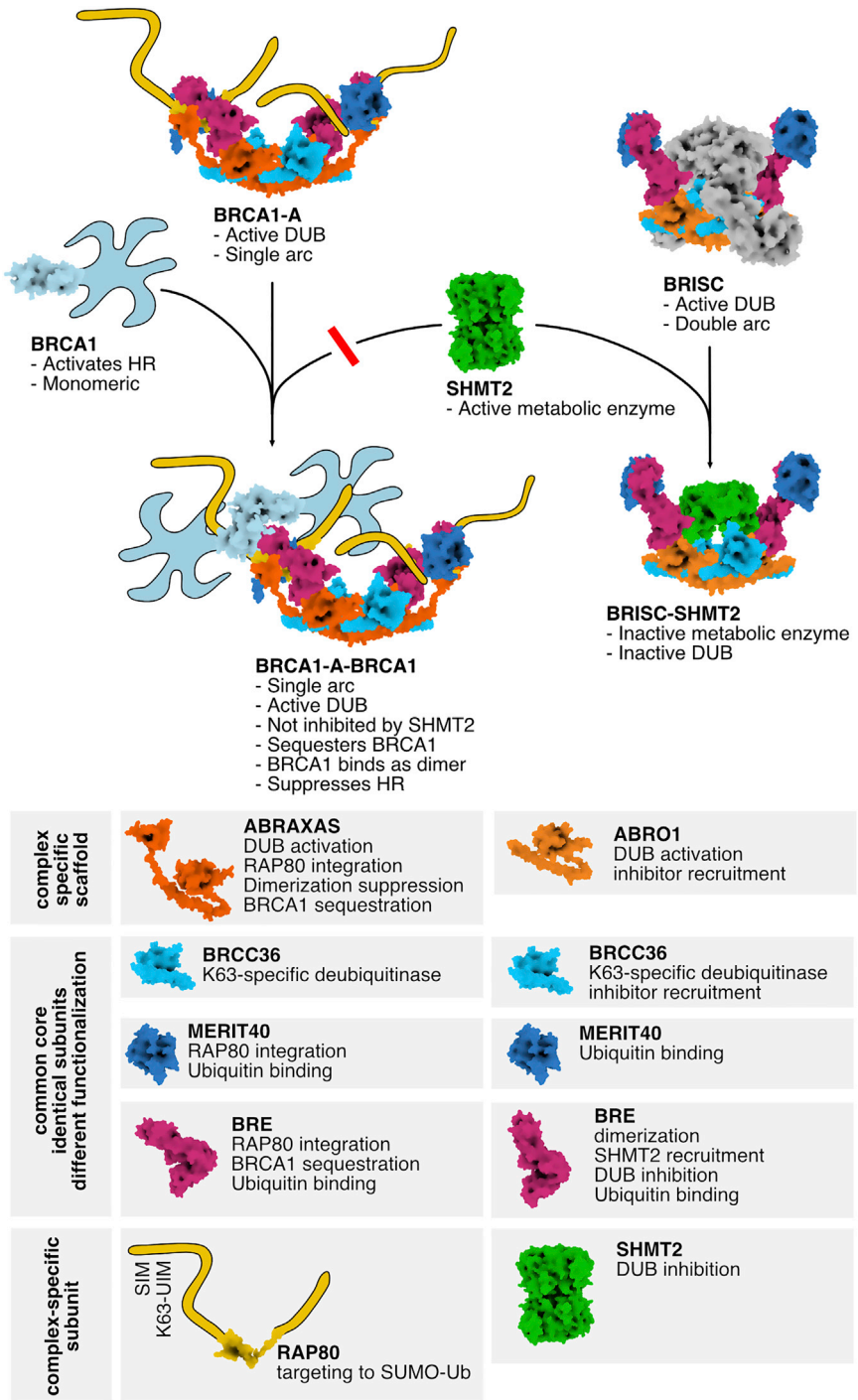

Figure 7. Assembly and Regulation of BRCA1-A and BRISC

Schematic summary of BRCA1-A and BRISC function.

The BRCA1-A complex is an important safeguard for genome stability, which is frequently mutated in inherited breast cancers. BRCA1-A serves three roles in DSB repair: (1) recruitment to foci by stable RAP80 integration (Kim et al., 2007; Sobhian et al., 2007; van Wijk et al., 2012; Wang et al., 2007), (2) delimiting the K63-Ub boundary around breaks (Ng et al., 2016), and (3) inhibiting resection by sequestering BRCA1 and limiting its availability for the BRCA1/2-PALB2-RAD51 complex (Goldstein and Kastan, 2015; Typas et al., 2015).

Our work demonstrates that ABRAXAS functionalizes BRCA1-A for all three tasks. We show that RAP80 is an integral, structural part of the BRCA1-A complex as it interacts not only with ABRAXAS, but has substantial interaction surfaces with two additional subunits, MERIT40 and BRE. Loss of MERIT40, or BRE, compromises BRCA1-A integrity and genome safeguarding, which is explained by the structure. Loss of the RAP80 SIM-UIM$_2$ domains gives rise to substantial deficiencies in BRCA1-A targeting to breaks and concomitant repair defects (Guzzo et al., 2012). The BRCA1-A architecture with the RAP80 SIM-UIM$_2$ domains bestows preferential recruitment to mixed SUMO/K63-Ub$_2$ chains. ABRAXAS recruits RAP80, and thereby localizes BRCA1-A to mixed chains, and likely interlinks K63-ubiquitin and SUMO signaling at repair sites and delimits the K63-ubiquitin boundary around breaks.

BRCA1-A plays an important role engaging and stabilizing BRCA1 at 2–10 kb distance from the breaks and inactivating it (Goldstein and Kastan, 2015; Typas et al., 2015). Binding of the BRCA1-BRCT domains to the ABRAXAS phospho-peptide is mutually incompatible with binding phosphorylated CtIP or BACH1 (CtIP: K_d~3.7 μM; BACH1: K_d~0.9 μM) (Shiozaki et al., 2004; Varma et al., 2005; Wu et al., 2016). The BRCA1-A arc architecture, with phosphorylation sites on ABRAXAS close to its C terminus, sequesters BRCA1 in a K_d ~60–80 nM complex, which is significantly tighter than the affinities reported for other BRCA1-BRCT interactions. Cradled distal from break sites within the high-affinity BRCA1-A scaffold contacting BRE and ABRAXAS, BRCA1 is unable to engage other activators of resection providing a structural rationale for the observed BRCA1 inhibition.

The BRCA1-A architecture provides the circuitry for BRCA1 sequestration and directed deubiquitination through distinct

structured modules. A mutation in BRCA1-BRCT (e.g., Lys1702-Met), which impairs ABRAXAS binding, gives rise to a hyper-resection phenotype equivalent to the loss of RAP80/BRCA1-A (Dever et al., 2011), demonstrating that both modules are essential for BRCA1-A function. BRCA1 sequestration and targeting to SUMO-ubiquitin marks critically depend on ABRAXAS yet at the same time involve other core subunits present in both BRISC and BRCA1-A.

The BRISC complex largely operates outside the nucleus, regulating K63-ubiquitin levels in immune signaling. Whether BRISC activity can be regulated was unclear previously. We find that in BRISC, it is also the subcomplex-specific subunit ABRO1 that functionalizes the complex, enabling SHMT2α binding. Cellular proteases are typically produced as inactive proenzymes (Khan and James, 1998), complexed to soluble proteinaceous inhibitors (Farady and Craik, 2010), or embedded in macromolecular complexes that are autoinhibited in the absence of a substrate (Lingaraju et al., 2014; Pathare et al., 2014; Worden et al., 2014; 2017). Overall, the MPN DUB family is a notable exception, with no soluble protein inhibitors described so far (Leznicki and Kulathu, 2017; Sahtoe et al., 2015; Vander Linden et al., 2015). While assembled BRISC and BRCA1-A complexes assume an active, non-autoinhibited, default state, BRISC binding to the soluble metabolic enzyme SHMT2α results in mutual inhibition of both SHMT2α and BRISC activity.

Endogenous co-purification (Sowa et al., 2009; Zheng et al., 2013) and subcellular co-localization of BRISC and SHMT2 establish that a reciprocally inhibited BRISC-SHMT2α complex forms in target cells. The interaction between SHMT2α and BRISC, and the ensuing inhibition, could be regulated, for example, through posttranslational modifications at the interface. How SHMT2α inhibition of BRISC can facilitate the reported BRISC-dependent deubiquitination of IFNAR1 presently remains unclear (Zheng et al., 2013). Combining the results of *in vitro* enzymatic studies and the reported variations in SHMT2α and ABRO1 levels across different human cell lines and tissues, we expect that the relative BRISC activity is impacted by SHMT2 levels in some tissues (e.g., in lymph nodes, colon, and liver) and is largely unaffected in others (e.g., in brain and reproductive organs) (Uhlén et al., 2015, 2017; Wilhelm et al., 2014). We predict inhibition to apply predominantly to the BRISC/DUB and not to the metabolic enzyme SHMT2, because SHMT2 is present in large (>10-fold) excess over BRISC in many tissues (Figure S6I). We note that cancer cells frequently increase reliance on one-carbon metabolism by overexpression of SHMT2 by >10-fold to adapt to the hypoxic conditions inside tumors (Amelio et al., 2014; Kim et al., 2015; Wilhelm et al., 2014) (Figure S7). Future work is needed to assess how SHMT2 expression affects K63-Ub homeostasis across different tissues in health and disease.

More than 20,000 ubiquitination sites in mammalian cells are deubiquitinated by a pool of ~100 DUBs (Leznicki and Kulathu, 2017; Mevissen and Komander, 2017). We find the BRCC36-containing BRCA1-A and BRISC complexes to be modular DUBs, with ABRAXAS and ABRO1 specifically integrating accessory factors RAP80, BRCA1, or SHMT2, respectively, and conferring targeting and regulation (Figure 7). Specific binding of these accessory factors is driven through interactions by the subcomplex-specific ABRO1/ABRAXAS subunits, combined with contacts by subunits shared between BRISC and BRCA1-A. Interestingly, it is the ABRO1 and ABRAXAS subunits that drive SHMT2 and RAP80/BRCA1 integration, respectively, but their integration involves additional contributions from the common core subunits. The BRISC/BRCA1-A structures and their functional dissection presented here reveal modularity in the MPN DUB family reminiscent to what has been described for ubiquitin ligases of the cullin-RING family (Petroski and Deshaies, 2005). We expect similar targeting and regulatory principles to apply to most multimeric DUB assemblies.

STAR★METHODS

Detailed methods are provided in the online version of this paper and include the following:

- KEY RESOURCES TABLE
- CONTACT FOR REAGENT AND RESOURCE SHARING
- EXPERIMENTAL MODEL AND SUBJECT DETAILS
  - Cell culture of human osteosarcoma (U2OS) cells
- METHOD DETAILS
  - Protein expression and purification of BRCA1-A and BRISC
  - BRCA1-A crystallization
  - BRCA1-A crystal structure determination
  - Protein expression and purification of SHMT2α
  - Cryo-electron microscopy
  - Image processing
  - Chain length specific degradation assay
  - Nuclear magnetic resonance experiments
  - $(Ub)_4$ pre-orientation assay
  - Cell biology and fluorescence microscopy of DNA repair foci
  - Co-expression in insect cells and pull-down
  - Analysis of RAP80 incorporation and double arc formation
  - Negative stain electron microscopy
  - Di-ubiquitin preparation
  - Preparation of SUMO/Ubiquitin mixed chains
  - SUMO/Ubiquitin mixed chains degradation assay
  - Protein expression and purification of BRCA1-BRCT
  - Sortase ligation of phosphorylated peptides to BRCA1-A
  - Microscale thermophoresis binding assays
  - Crosslinking mass spectrometry
  - Bio-layer interferometry
  - Internally quenched fluorophore (IQF) deubiquitination assays
  - Quantitative fluorescence microscopy of ABRO1 and SHMT2
- QUANTIFICATION AND STATISTICAL ANALYSIS
- DATA AND SOFTWARE AVAILABILITY

SUPPLEMENTAL INFORMATION

Supplemental Information can be found online at https://doi.org/10.1016/j.molcel.2019.06.002.

ACKNOWLDEGEMENTS

We gratefully acknowledge the support of the FMI core facilities: D. Hess, V. Iesmantavicius, and J. Seebacher (Proteomics and Protein Analysis Facility) for mass spectrometry; H.R. Hotz (Computational Biology Platform) for phylogenetics; A. Graff Meyer and C. Genoud (Facility for Advanced Imaging and Microscopy) for microscopy; J. Keusch (Protein Structure Facility) for crystallization facilities. For sharing material, we thank D. Durocher (RAP80 knockout U2OS cells), A. Jetten (GFP-RAP80 construct), and T. Blundell (BRCA1-BRCT construct). We acknowledge the Paul Scherrer Institut, Villigen, Switzerland for access to beamline X06SA (PXI) of the Swiss Light Source and thank M. Wang for assistance.

J.R. was funded by a Novartis Presidential Fellowship and C.G. by the Danish Cancer Society (grant no. R146-RP11394). This work was funded by the Novartis Research Foundation (M.E.G., A.H.F.M.P.), NWO-VENI (863.11.007) and NWO-VIDI (016.161.320) grants to M.S.L., a Consolidator grant from the European Research Council (ERC-CoG) to H.v.A., NIH grants R01 GM124148 and R01 GM127707 to S.M.R., the Lundbeck Foundation (N.M.), a Senior Investigator Award from the Wellcome Trust (098391/Z/12/7) to E.B. and R.T.H., and the Swiss National Science Foundation through Sinergia grant number CRSII3_160734/1 and by the European Research Council under the European Union's Horizon 2020 Research and Innovation program grant agreement, grant number 666068, to N.H.T.

AUTHOR CONTRIBUTIONS

Conceptualization, J.R. and N.H.T.; Methodology, J.R., R.D.B., A.D.S., S.C., M.S.L., H.v.A., A.F.M.I., A.H.M., C.G., U.H., and L.G.; Validation, J.R. and N.H.T.; Formal Analysis, J.R., R.D.B., A.D.S., S.C., A.A.-P., M.S.L., A.H.M., U.H., and L.G.; Investigation, J.R., R.D.B., A.D.S., S.C., M.E.G., W.A., A.A.-P., M.S.L., A.F.M.I., A.H.M., and C.G.; Resources, J.R., W.A., A.A.-P., A.F.M.I., E.B., J.D.A., C.G., T.B., and M.R.; Data Curation, J.R., R.D.B., A.D.S., and S.C.; Writing – Original Draft, J.R. and N.H.T.; Writing – Review and Editing, J.R., R.D.B., and N.H.T.; Visualization, J.R., R.D.B., A.D.S., S.C., M.E.G., A.A.-P., M.S.L., H.v.A. and A.H.M.; Supervision, N.H.T.; Project Administration, J.R. and N.H.T.; Funding Acquisition, A.H.F.M.P., S.M.R., N.M., M.S.L., H.v.A., R.T.H., and N.H.T.

DECLARATION OF INTEREST

The authors declare no competing interests.

Received: January 24, 2019
Revised: April 30, 2019
Accepted: May 31, 2019
Published: June 25, 2019

SUPPORTING CITATIONS

The following references appear in the Supplemental Information: Chaneton et al. (2012); Putnam et al. (2008); Wishart et al. (2018).

REFERENCES

Adams, P.D., Afonine, P.V., Bunkóczi, G., Chen, V.B., Davis, I.W., Echols, N., Headd, J.J., Hung, L.-W., Kapral, G.J., Grosse-Kunstleve, R.W., et al. (2010). PHENIX: a comprehensive Python-based system for macromolecular structure solution. Acta Crystallogr. D Biol. Crystallogr. *66*, 213–221.

Ambivero, C.T., Cilenti, L., and Zervos, A.S. (2012). ATF4 interacts with Abro1/KIAA0157 scaffold protein and participates in a cytoprotective pathway. Biochim. Biophys. Acta *1823*, 2149–2156.

Amelio, I., Cutruzzolá, F., Antonov, A., Agostini, M., and Melino, G. (2014). Serine and glycine metabolism in cancer. Trends Biochem. Sci. *39*, 191–198.

Anderson, D.D., and Stover, P.J. (2009). SHMT1 and SHMT2 are functionally redundant in nuclear de novo thymidylate biosynthesis. PLoS ONE *4*, e5839.

Badgujar, D.C., Sawant, U., Yadav, L., Hosur, M.V., and Varma, A.K.; Vikrant (2013). Preliminary crystallographic studies of BRCA1 BRCT-ABRAXAS complex. Acta Crystallogr. Sect. F Struct. Biol. Cryst. Commun. *69*, 1401–1404.

Bett, J.S., Ritorto, M.S., Ewan, R., Jaffray, E.G., Virdee, S., Chin, J.W., Knebel, A., Kurz, T., Trost, M., Tatham, M.H., and Hay, R.T. (2015). Ubiquitin C-terminal hydrolases cleave isopeptide- and peptide-linked ubiquitin from structured proteins but do not edit ubiquitin homopolymers. Biochem. J. *466*, 489–498.

Bian, C., Wu, R., Cho, K., and Yu, X. (2012). Loss of BRCA1-A complex function in RAP80 null tumor cells. PLoS ONE *7*, e40406.

Brown, N.G., VanderLinden, R., Watson, E.R., Qiao, R., Grace, C.R.R., Yamaguchi, M., Weissmann, F., Frye, J.J., Dube, P., Ei Cho, S., et al. (2015). RING E3 mechanism for ubiquitin ligation to a disordered substrate visualized for human anaphase-promoting complex. Proc. Natl. Acad. Sci. USA *112*, 5272–5279.

Chaneton, B., Hillmann, P., Zheng, L., Martin, A.C.L., Maddocks, O.D.K., Chokkathukalam, A., Coyle, J.E., Jankevics, A., Holding, F.P., Vousden, K.H., et al. (2012). Serine is a natural ligand and allosteric activator of pyruvate kinase M2. Nature *491*, 458–462.

Chen, V.B., Arendall, W.B., 3rd, Headd, J.J., Keedy, D.A., Immormino, R.M., Kapral, G.J., Murray, L.W., Richardson, J.S., and Richardson, D.C. (2010). MolProbity: all-atom structure validation for macromolecular crystallography. Acta Crystallogr. D Biol. Crystallogr. *66*, 12–21.

Cilenti, L., Balakrishnan, M.P., Wang, X.-L., Ambivero, C., Sterlicchi, M., del Monte, F., Ma, X.L., and Zervos, A.S. (2011). Regulation of Abro1/KIAA0157 during myocardial infarction and cell death reveals a novel cardioprotective mechanism for Lys63-specific deubiquitination. J. Mol. Cell. Cardiol. *50*, 652–661.

Clapperton, J.A., Manke, I.A., Lowery, D.M., Ho, T., Haire, L.F., Yaffe, M.B., and Smerdon, S.J. (2004). Structure and mechanism of BRCA1 BRCT domain recognition of phosphorylated BACH1 with implications for cancer. Nat. Struct. Mol. Biol. *11*, 512–518.

Coleman, K.A., and Greenberg, R.A. (2011). The BRCA1-RAP80 complex regulates DNA repair mechanism utilization by restricting end resection. J. Biol. Chem. *286*, 13669–13680.

Cooper, E.M., Cutcliffe, C., Kristiansen, T.Z., Pandey, A., Pickart, C.M., and Cohen, R.E. (2009). K63-specific deubiquitination by two JAMM/MPN+ complexes: BRISC-associated Brcc36 and proteasomal Poh1. EMBO J. *28*, 621–631.

Cowtan, K. (2000). General quadratic functions in real and reciprocal space and their application to likelihood phasing. Acta Crystallogr. D Biol. Crystallogr. *56*, 1612–1621.

Cowtan, K. (2010). Recent developments in classical density modification. Acta Crystallogr. D Biol. Crystallogr. *66*, 470–478.

Croll, T.I. (2018). ISOLDE: a physically realistic environment for model building into low-resolution electron-density maps. Acta Crystallogr. D Struct. Biol. *74*, 519–530.

Delaglio, F., Grzesiek, S., Vuister, G.W., Zhu, G., Pfeifer, J., and Bax, A. (1995). NMRPipe: a multidimensional spectral processing system based on UNIX pipes. J. Biomol. NMR *6*, 277–293.

Dever, S.M., Golding, S.E., Rosenberg, E., Adams, B.R., Idowu, M.O., Quillin, J.M., Valerie, N., Xu, B., Povirk, L.F., and Valerie, K. (2011). Mutations in the BRCT binding site of BRCA1 result in hyper-recombination. Aging (Albany N.Y.) *3*, 515–532.

Ducker, G.S., Ghergurovich, J.M., Mainolfi, N., Suri, V., Jeong, S.K., Hsin-Jung Li, S., Friedman, A., Manfredi, M.G., Gitai, Z., Kim, H., and Rabinowitz, J.D. (2017). Human SHMT inhibitors reveal defective glycine import as a targetable metabolic vulnerability of diffuse large B-cell lymphoma. Proc. Natl. Acad. Sci. USA *114*, 11404–11409.

Emsley, P., Lohkamp, B., Scott, W.G., and Cowtan, K. (2010). Features and development of Coot. Acta Crystallogr. D Biol. Crystallogr. *66*, 486–501.

Evans, P.R. (2011). An introduction to data reduction: space-group determination, scaling and intensity statistics. Acta Crystallogr. D Biol. Crystallogr. *67*, 282–292.

Evans, P.R., and Murshudov, G.N. (2013). How good are my data and what is the resolution? Acta Crystallogr. D Biol. Crystallogr. *69*, 1204–1214.

Farady, C.J., and Craik, C.S. (2010). Mechanisms of macromolecular protease inhibitors. ChemBioChem *11*, 2341–2346.

Feng, L., Huang, J., and Chen, J. (2009). MERIT40 facilitates BRCA1 localization and DNA damage repair. Genes Dev. *23*, 719–728.

Feng, L., Wang, J., and Chen, J. (2010). The Lys63-specific deubiquitinating enzyme BRCC36 is regulated by two scaffold proteins localizing in different subcellular compartments. J. Biol. Chem. *285*, 30982–30988.

Giardina, G., Brunotti, P., Fiascarelli, A., Cicalini, A., Costa, M.G.S., Buckle, A.M., di Salvo, M.L., Giorgi, A., Marani, M., Paone, A., et al. (2015). How pyridoxal 5′-phosphate differentially regulates human cytosolic and mitochondrial serine hydroxymethyltransferase oligomeric state. FEBS J. *282*, 1225–1241.

Goldstein, M., and Kastan, M.B. (2015). Repair versus checkpoint functions of BRCA1 are differentially regulated by site of chromatin binding. Cancer Res. *75*, 2699–2707.

Guimaraes, C.P., Witte, M.D., Theile, C.S., Bozkurt, G., Kundrat, L., Blom, A.E.M., and Ploegh, H.L. (2013). Site-specific C-terminal and internal loop labeling of proteins using sortase-mediated reactions. Nat. Protoc. *8*, 1787–1799.

Guzzo, C.M., Berndsen, C.E., Zhu, J., Gupta, V., Datta, A., Greenberg, R.A., Wolberger, C., and Matunis, M.J. (2012). RNF4-dependent hybrid SUMO-ubiquitin chains are signals for RAP80 and thereby mediate the recruitment of BRCA1 to sites of DNA damage. Sci. Signal. *5*, ra88.

Hein, M.Y., Hubner, N.C., Poser, I., Cox, J., Nagaraj, N., Toyoda, Y., Gak, I.A., Weisswange, I., Mansfeld, J., Buchholz, F., et al. (2015). A human interactome in three quantitative dimensions organized by stoichiometries and abundances. Cell *163*, 712–723.

Hicke, L., Schubert, H.L., and Hill, C.P. (2005). Ubiquitin-binding domains. Nat. Rev. Mol. Cell Biol. *6*, 610–621.

Hodson, C., Cole, A.R., Lewis, L.P.C., Miles, J.A., Purkiss, A., and Walden, H. (2011). Structural analysis of human FANCL, the E3 ligase in the Fanconi anemia pathway. J. Biol. Chem. *286*, 32628–32637.

Hu, X., Kim, J.A., Castillo, A., Huang, M., Liu, J., and Wang, B. (2011a). NBA1/MERIT40 and BRE interaction is required for the integrity of two distinct deubiquitinating enzyme BRCC36-containing complexes. J. Biol. Chem. *286*, 11734–11745.

Hu, Y., Scully, R., Sobhian, B., Xie, A., Shestakova, E., and Livingston, D.M. (2011b). RAP80-directed tuning of BRCA1 homologous recombination function at ionizing radiation-induced nuclear foci. Genes Dev. *25*, 685–700.

Hu, X., Paul, A., and Wang, B. (2012). Rap80 protein recruitment to DNA double-strand breaks requires binding to both small ubiquitin-like modifier (SUMO) and ubiquitin conjugates. J. Biol. Chem. *287*, 25510–25519.

Joosten, R.P., Long, F., Murshudov, G.N., and Perrakis, A. (2014). The PDB_REDO server for macromolecular structure model optimization. IUCrJ *1*, 213–220.

Kabsch, W. (2010). XDS. Acta Crystallogr. D Biol. Crystallogr. *66*, 125–132.

Kakarougkas, A., Ismail, A., Katsuki, Y., Freire, R., Shibata, A., and Jeggo, P.A. (2013). Co-operation of BRCA1 and POH1 relieves the barriers posed by 53BP1 and RAP80 to resection. Nucleic Acids Res. *41*, 10298–10311.

Kastner, B., Fischer, N., Golas, M.M., Sander, B., Dube, P., Boehringer, D., Hartmuth, K., Deckert, J., Hauer, F., Wolf, E., et al. (2008). GraFix: sample preparation for single-particle electron cryomicroscopy. Nat. Methods *5*, 53–55.

Khan, A.R., and James, M.N. (1998). Molecular mechanisms for the conversion of zymogens to active proteolytic enzymes. Protein Sci. *7*, 815–836.

Kim, H., Chen, J., and Yu, X. (2007). Ubiquitin-binding protein RAP80 mediates BRCA1-dependent DNA damage response. Science *316*, 1202–1205.

Kim, D., Fiske, B.P., Birsoy, K., Freinkman, E., Kami, K., Possemato, R.L., Chudnovsky, Y., Pacold, M.E., Chen, W.W., Cantor, J.R., et al. (2015). SHMT2 drives glioma cell survival in ischaemia but imposes a dependence on glycine clearance. Nature *520*, 363–367.

Kucukelbir, A., Sigworth, F.J., and Tagare, H.D. (2014). Quantifying the local resolution of cryo-EM density maps. Nat. Methods *11*, 63–65.

Kuzmič, P. (2009). DynaFit–a software package for enzymology. Methods Enzymol. *467*, 247–280.

Kyrieleis, O.J.P., McIntosh, P.B., Webb, S.R., Calder, L.J., Lloyd, J., Patel, N.A., Martin, S.R., Robinson, C.V., Rosenthal, P.B., and Smerdon, S.J. (2016). Three-dimensional architecture of the human BRCA1-A histone deubiquitinase core complex. Cell Rep. *17*, 3099–3106.

Lee, G.Y., Haverty, P.M., Li, L., Kljavin, N.M., Bourgon, R., Lee, J., Stern, H., Modrusan, Z., Seshagiri, S., Zhang, Z., et al. (2014). Comparative oncogenomics identifies PSMB4 and SHMT2 as potential cancer driver genes. Cancer Res. *74*, 3114–3126.

Leznicki, P., and Kulathu, Y. (2017). Mechanisms of regulation and diversification of deubiquitylating enzyme function. J. Cell Sci. *130*, 1997–2006.

Li, X., Mooney, P., Zheng, S., Booth, C.R., Braunfeld, M.B., Gubbens, S., Agard, D.A., and Cheng, Y. (2013). Electron counting and beam-induced motion correction enable near-atomic-resolution single-particle cryo-EM. Nat. Methods *10*, 584–590.

Lingaraju, G.M., Bunker, R.D., Cavadini, S., Hess, D., Hassiepen, U., Renatus, M., Fischer, E.S., and Thomä, N.H. (2014). Crystal structure of the human COP9 signalosome. Nature *512*, 161–165.

Liu, X., and Ladias, J.A.A. (2013). Structural basis for the BRCA1 BRCT interaction with the proteins ATRIP and BAAT1. Biochemistry *52*, 7618–7627.

Lombardi, P.M., Matunis, M.J., and Wolberger, C. (2017). RAP80, ubiquitin and SUMO in the DNA damage response. J. Mol. Med. (Berl.) *95*, 799–807.

McCoy, A.J., Grosse-Kunstleve, R.W., Adams, P.D., Winn, M.D., Storoni, L.C., and Read, R.J. (2007). Phaser crystallographic software. J. Appl. Cryst. *40*, 658–674.

Mevissen, T.E.T., and Komander, D. (2017). Mechanisms of deubiquitinase specificity and regulation. Annu. Rev. Biochem. *86*, 159–192.

Mok, M.T.S., and Henderson, B.R. (2012). The in vivo dynamic organization of BRCA1-A complex proteins at DNA damage-induced nuclear foci. Traffic *13*, 800–814.

Ng, H.-M., Wei, L., Lan, L., and Huen, M.S.Y. (2016). The Lys63-deubiquitylating enzyme BRCC36 limits DNA break processing and repair. J. Biol. Chem. *291*, 16197–16207.

Nicholls, R.A., Long, F., and Murshudov, G.N. (2012). Low-resolution refinement tools in REFMAC5. Acta Crystallogr. D Biol. Crystallogr. *68*, 404–417.

Nikkilä, J., Coleman, K.A., Morrissey, D., Pylkäs, K., Erkko, H., Messick, T.E., Karppinen, S.-M., Amelina, A., Winqvist, R., and Greenberg, R.A. (2009). Familial breast cancer screening reveals an alteration in the RAP80 UIM domain that impairs DNA damage response function. Oncogene *28*, 1843–1852.

Pathare, G.R., Nagy, I., Śledź, P., Anderson, D.J., Zhou, H.-J., Pardon, E., Steyaert, J., Förster, F., Bracher, A., and Baumeister, W. (2014). Crystal structure of the proteasomal deubiquitylation module Rpn8-Rpn11. Proc. Natl. Acad. Sci. USA *111*, 2984–2989.

Patterson-Fortin, J., Shao, G., Bretscher, H., Messick, T.E., and Greenberg, R.A. (2010). Differential regulation of JAMM domain deubiquitinating enzyme activity within the RAP80 complex. J. Biol. Chem. *285*, 30971–30981.

Pei, J., Kim, B.-H., and Grishin, N.V. (2008). PROMALS3D: a tool for multiple protein sequence and structure alignments. Nucleic Acids Research *36*, 2295–2300.

Petroski, M.D., and Deshaies, R.J. (2005). Function and regulation of cullin-RING ubiquitin ligases. Nat. Rev. Mol. Cell Biol. *6*, 9–20.

Plechanovová, A., Jaffray, E.G., McMahon, S.A., Johnson, K.A., Navrátilová, I., Naismith, J.H., and Hay, R.T. (2011). Mechanism of ubiquitylation by dimeric RING ligase RNF4. Nat. Struct. Mol. Biol. *18*, 1052–1059.

Putnam, N.H., Butts, T., Ferrier, D.E.K., Furlong, R.F., Hellsten, U., Kawashima, T., Robinson-Rechavi, M., Shoguchi, E., Terry, A., Yu, J.-K., et al. (2008). The amphioxus genome and the evolution of the chordate karyotype. Nature *453*, 1064–1071.

Py, B.F., Kim, M.-S., Vakifahmetoglu-Norberg, H., and Yuan, J. (2013). Deubiquitination of NLRP3 by BRCC3 critically regulates inflammasome activity. Mol. Cell *49*, 331–338.

Ray, H., Moreau, K., Dizin, E., Callebaut, I., and Venezia, N.D. (2006). ACCA phosphopeptide recognition by the BRCT repeats of BRCA1. J. Mol. Biol. *359*, 973–982.

Rebbeck, T.R., Mitra, N., Domchek, S.M., Wan, F., Friebel, T.M., Tran, T.V., Singer, C.F., Tea, M.K.M., Blum, J.L., Tung, N., et al.; Epidemiological Study of BRCA1 and BRCA2 Mutation Carriers (EMBRACE) (2011). Modification of BRCA1-associated breast and ovarian cancer risk by BRCA1-interacting genes. Cancer Res. *71*, 5792–5805.

Riedinger, C., Boehringer, J., Trempe, J.F., Lowe, E.D., Brown, N.R., Gehring, K., Noble, M.E.M., Gordon, C., and Endicott, J.A. (2010). Structure of Rpn10 and its interactions with polyubiquitin chains and the proteasome subunit Rpn12. J. Biol. Chem. *285*, 33992–34003.

Rosenthal, P.B., and Henderson, R. (2003). Optimal determination of particle orientation, absolute hand, and contrast loss in single-particle electron cryomicroscopy. J. Mol. Biol. *333*, 721–745.

Sahtoe, D.D., van Dijk, W.J., El Oualid, F., Ekkebus, R., Ovaa, H., and Sixma, T.K. (2015). Mechanism of UCH-L5 activation and inhibition by DEUBAD domains in RPN13 and INO80G. Mol. Cell *57*, 887–900.

Sato, Y., Yoshikawa, A., Yamagata, A., Mimura, H., Yamashita, M., Ookata, K., Nureki, O., Iwai, K., Komada, M., and Fukai, S. (2008). Structural basis for specific cleavage of Lys 63-linked polyubiquitin chains. Nature *455*, 358–362.

Scheres, S.H.W. (2012). RELION: implementation of a Bayesian approach to cryo-EM structure determination. J. Struct. Biol. *180*, 519–530.

Schindelin, J., Arganda-Carreras, I., Frise, E., Kaynig, V., Longair, M., Pietzsch, T., Preibisch, S., Rueden, C., Saalfeld, S., Schmid, B., et al. (2012). Fiji: an open-source platform for biological-image analysis. Nat. Methods *9*, 676–682.

Schneider, C.A., Rasband, W.S., and Eliceiri, K.W. (2012). NIH Image to ImageJ: 25 years of image analysis. Nat. Methods *9*, 671–675.

Schröder, G.F., Levitt, M., and Brunger, A.T. (2010). Super-resolution biomolecular crystallography with low-resolution data. Nature *464*, 1218–1222.

Shao, G., Patterson-Fortin, J., Messick, T.E., Feng, D., Shanbhag, N., Wang, Y., and Greenberg, R.A. (2009). MERIT40 controls BRCA1-Rap80 complex integrity and recruitment to DNA double-strand breaks. Genes Dev. *23*, 740–754.

Sheldrick, G.M. (2008). A short history of SHELX. Acta Crystallogr. A *64*, 112–122.

Shiozaki, E.N., Gu, L., Yan, N., and Shi, Y. (2004). Structure of the BRCT repeats of BRCA1 bound to a BACH1 phosphopeptide: implications for signaling. Mol. Cell *14*, 405–412.

Sobhian, B., Shao, G., Lilli, D.R., Culhane, A.C., Moreau, L.A., Xia, B., Livingston, D.M., and Greenberg, R.A. (2007). RAP80 targets BRCA1 to specific ubiquitin structures at DNA damage sites. Science *316*, 1198–1202.

Solyom, S., Aressy, B., Pylkäs, K., Patterson-Fortin, J., Hartikainen, J.M., Kallioniemi, A., Kauppila, S., Nikkilä, J., Kosma, V.-M., Mannermaa, A., et al. (2012). Breast cancer-associated Abraxas mutation disrupts nuclear localization and DNA damage response functions. Sci. Transl. Med. *4*, 122ra23.

Sowa, M.E., Bennett, E.J., Gygi, S.P., and Harper, J.W. (2009). Defining the human deubiquitinating enzyme interaction landscape. Cell *138*, 389–403.

Studier, F.W. (2005). Protein production by auto-induction in high density shaking cultures. Protein Expr. Purif. *41*, 207–234.

Tang, G., Peng, L., Baldwin, P.R., Mann, D.S., Jiang, W., Rees, I., and Ludtke, S.J. (2007). EMAN2: an extensible image processing suite for electron microscopy. J. Struct. Biol. *157*, 38–46.

Typas, D., Luijsterburg, M.S., Wiegant, W.W., Diakatou, M., Helfricht, A., Thijssen, P.E., van den Broek, B., Mullenders, L.H., and van Attikum, H. (2015). The de-ubiquitylating enzymes USP26 and USP37 regulate homologous recombination by counteracting RAP80. Nucleic Acids Res. *43*, 6919–6933.

Uckelmann, M., and Sixma, T.K. (2017). Histone ubiquitination in the DNA damage response. DNA Repair (Amst.) *56*, 92–101.

Uhlén, M., Fagerberg, L., Hallström, B.M., Lindskog, C., Oksvold, P., Mardinoglu, A., Sivertsson, Å., Kampf, C., Sjöstedt, E., Asplund, A., et al. (2015). Proteomics. Tissue-based map of the human proteome. Science *347*, 1260419.

Uhlén, M., Zhang, C., Lee, S., Sjöstedt, E., Fagerberg, L., Bidkhori, G., Benfeitas, R., Arif, M., Liu, Z., Edfors, F., et al. (2017). A pathology atlas of the human cancer transcriptome. Science *357*, 357.

van Wijk, S.J.L., Fiskin, E., Putyrski, M., Pampaloni, F., Hou, J., Wild, P., Kensche, T., Grecco, H.E., Bastiaens, P., and Dikic, I. (2012). Fluorescence-based sensors to monitor localization and functions of linear and K63-linked ubiquitin chains in cells. Mol. Cell *47*, 797–809.

Vander Linden, R.T., Hemmis, C.W., Schmitt, B., Ndoja, A., Whitby, F.G., Robinson, H., Cohen, R.E., Yao, T., and Hill, C.P. (2015). Structural basis for the activation and inhibition of the UCH37 deubiquitylase. Mol. Cell *57*, 901–911.

Varma, A.K., Brown, R.S., Birrane, G., and Ladias, J.A.A. (2005). Structural basis for cell cycle checkpoint control by the BRCA1-CtIP complex. Biochemistry *44*, 10941–10946.

Wang, B., Matsuoka, S., Ballif, B.A., Zhang, D., Smogorzewska, A., Gygi, S.P., and Elledge, S.J. (2007). Abraxas and RAP80 form a BRCA1 protein complex required for the DNA damage response. Science *316*, 1194–1198.

Wang, B., Hurov, K., Hofmann, K., and Elledge, S.J. (2009). NBA1, a new player in the Brca1 A complex, is required for DNA damage resistance and checkpoint control. Genes Dev. *23*, 729–739.

Wang, R.Y.-R., Song, Y., Barad, B.A., Cheng, Y., Fraser, J.S., and DiMaio, F. (2016). Automated structure refinement of macromolecular assemblies from cryo-EM maps using Rosetta. eLife *5*, 352.

Wilhelm, M., Schlegl, J., Hahne, H., Gholami, A.M., Lieberenz, M., Savitski, M.M., Ziegler, E., Butzmann, L., Gessulat, S., Marx, H., et al. (2014). Mass-spectrometry-based draft of the human proteome. Nature *509*, 582–587.

Winn, M.D., Ballard, C.C., Cowtan, K.D., Dodson, E.J., Emsley, P., Evans, P.R., Keegan, R.M., Krissinel, E.B., Leslie, A.G.W., McCoy, A., et al. (2011). Overview of the CCP4 suite and current developments. Acta Crystallogr. D Biol. Crystallogr. *67*, 235–242.

Winter, G., Waterman, D.G., Parkhurst, J.M., Brewster, A.S., Gildea, R.J., Gerstel, M., Fuentes-Montero, L., Vollmar, M., Michels-Clark, T., Young, I.D., et al. (2018). DIALS: implementation and evaluation of a new integration package. Acta Crystallogr. D Struct. Biol. *74*, 85–97.

Wishart, D.S., Feunang, Y.D., Marcu, A., Guo, A.C., Liang, K., Vázquez-Fresno, R., Sajed, T., Johnson, D., Li, C., Karu, N., et al. (2018). HMDB 4.0: the human metabolome database for 2018. Nucleic Acids Res. *46* (D1), D608–D617.

Worden, E.J., Padovani, C., and Martin, A. (2014). Structure of the Rpn11-Rpn8 dimer reveals mechanisms of substrate deubiquitination during proteasomal degradation. Nat. Struct. Mol. Biol. *21*, 220–227.

Worden, E.J., Dong, K.C., and Martin, A. (2017). An AAA motor-driven mechanical switch in Rpn11 controls deubiquitination at the 26S proteasome. Mol. Cell *67*, 799–811.e8.

Wu, J., Liu, C., Chen, J., and Yu, X. (2012). RAP80 protein is important for genomic stability and is required for stabilizing BRCA1-A complex at DNA damage sites in vivo. J. Biol. Chem. *287*, 22919–22926.

Wu, Q., Paul, A., Su, D., Mehmood, S., Foo, T.K., Ochi, T., Bunting, E.L., Xia, B., Robinson, C.V., Wang, B., and Blundell, T.L. (2016). Structure of BRCA1-BRCT/Abraxas complex reveals phosphorylation-dependent BRCT dimerization at DNA damage sites. Mol. Cell *61*, 434–448.

Xu, M., Moresco, J.J., Chang, M., Mukim, A., Smith, D., Diedrich, J.K., Yates, J.R., 3rd, and Jones, K.A. (2018). SHMT2 and the BRCC36/BRISC deubiquitinase regulate HIV-1 Tat K63-ubiquitylation and destruction by autophagy. PLoS Pathog. *14*, e1007071–e22.

Yan, Z., Kim, Y.-S., and Jetten, A.M. (2002). RAP80, a novel nuclear protein that interacts with the retinoid-related testis-associated receptor. J. Biol. Chem. *277*, 32379–32388.

Yin, Z., Menendez, D., Resnick, M.A., French, J.E., Janardhan, K.S., and Jetten, A.M. (2012). RAP80 is critical in maintaining genomic stability and suppressing tumor development. Cancer Res. *72*, 5080–5090.

Zeqiraj, E., Tian, L., Piggott, C.A., Pillon, M.C., Duffy, N.M., Ceccarelli, D.F., Keszei, A.F.A., Lorenzen, K., Kurinov, I., Orlicky, S., et al. (2015). Higher-order assembly of BRCC36-KIAA0157 is required for DUB activity and biological function. Mol. Cell *59*, 970–983.

Zhang, K. (2016). Gctf: Real-time CTF determination and correction. J. Struct. Biol. *193*, 1–12.

Zheng, H., Gupta, V., Patterson-Fortin, J., Bhattacharya, S., Katlinski, K., Wu, J., Varghese, B., Carbone, C.J., Aressy, B., Fuchs, S.Y., and Greenberg, R.A. (2013). A BRISC-SHMT complex deubiquitinates IFNAR1 and regulates interferon responses. Cell Rep. *5*, 180–193.

STAR★METHODS

KEY RESOURCES TABLE

REAGENT or RESOURCE	SOURCE	IDENTIFIER
Antibodies		
Mouse monoclonal anti-BRCA1	Santa Cruz Biotechnology	Cat# sc-6954; RRID: AB_626761
Rabbit anti-MDC1	Abcam	Cat# ab11171; RRID: AB_297810
Rabbit anti-RAP80	Bethyl Laboratories	Cat# A300-764; RRID: AB_2779443
Mouse anti-GFP	Roche	Cat# 11814460001; RRID: AB_390913
Mouse anti-tubulin	Sigma-Aldrich	Cat# T6199; RRID: AB_477583
Rabbit anti-SHMT2	Sigma-Aldrich	Cat# SAB1100388; RRID: AB_10610173
Rabbit anti-ABRO1	Abcam	Cat# ab74333; RRID: AB_1280902
Alexa Fluor 488-conjugated donkey anti-rabbit antibody	ThermoFisher	Cat# R37118; RRID: AB_2536183
Bacterial and Virus Strains		
Escherichia coli BL21-CodonPlus (DE3)-RIL	Agilent Technologies	Cat# 230245
Chemicals, Peptides, and Recombinant Proteins		
SigmaFast protease inhibitor cocktail	Sigma-Aldrich	Cat# S8820
Strep-Tactin resin	iba	Cat# 2-1201-025
TEV protease	This paper	N/A
Human and mouse BRCA1-A complexes	This paper	N/A
Human and mouse BRISC complexes	This paper	N/A
K63-linked di-ubiquitin (K63-diUb)	Emma Branigan, Ronald T. Hay	N/A
SUMO-2-K63-$(Ub)_2$	Emma Branigan, Ronald T. Hay	N/A
K63-$(Ub)_2$	Boston Biochem	Cat# UC-300B
K63-$(Ub)_3$	Boston Biochem	Cat# UC-315B
K63-$(Ub)_4$	Boston Biochem	Cat# UC-310B
peptide p-Ser404 (GGGFGEYpSRSPTF)	Biomatik	Custom synthesis
Peptide p-Ser406 (GGGFGEYSRpSPTF	Biomatik	Custom synthesis
peptides p-Ser404/406 (GGGFGEYpSRpSPTF)	Biomatik	Custom synthesis
BirA enzyme	This paper	N/A
MitoTracker Red CMXRos	Thermo Fisher Scientific	Cat# M7512
Alexa Fluor 633-conjugated wheat germ agglutinin	Thermo Fisher Scientific	Cat# W21404
K63-$(Ub)_4$, TAMRA label on proximal ubiquitin	LifeSensors	Cat# SI6304T
K63-$(Ub)_4$, TAMRA label on distal ubiquitin	Boston Biochem	Custom synthesis
Critical Commercial Assays		
IQF DiUb K63 assay	Life Sensors	Cat# DU0102, DU6301
Deposited Data		
Original image files	This paper; Mendeley Data	https://dx.doi.org/10.17632/8ntswhp8d5.1
Structure of BRCA1-A complex	This paper	PDB: 6GVW
Map of BRISC-SHMT2 complex	This paper	EMDB: EMDB-0132
Structure of BRISC-SHMT2 complex	This paper	PDB: 6H3C
PLP-bound SHMT2 structure	Giardina et al., 2015	PDB: 5V7I
Apo-SHMT2	Unpublished data	PDB: 6DK3
COP9 signalosome	Lingaraju et al., 2014	PDB: 4D10
APC2-UBCH10 complex	Brown et al., 2015	PDB: 4YII
Crystal Structure of the SpRpn10 VWA domain	Riedinger et al., 2010	PDB: 2X5N
Structure of CfBRCC36-CfKIAA0157 complex	Zeqiraj et al., 2015	PDB: 5CW3

(*Continued on next page*)

Continued

REAGENT or RESOURCE	SOURCE	IDENTIFIER
Experimental Models: Cell Lines		
Spodoptera frugiperda Sf9 cells	Thermo Fisher Scientific	Cat# 11496015
Tni insect cells	Expression Systems	Cat# 94-002F
Human osteosarcoma (U2OS) cells	Dr. Durocher	N/A
U2OS Rap80-KO	Dr. Durocher	N/A
HEK293T	Dr. Peters	N/A
Recombinant DNA		
pFastBac MmABRAXAS	This paper	N/A
pFastBac MmABRO1	This paper	N/A
pFastBac MmBRCC36	This paper	N/A
pFastBac MmBRE	This paper	N/A
pFastBac MmMERIT40	This paper	N/A
pFastBac MmRAP80	This paper	N/A
pFastBac MmRAP80 250-413	This paper	N/A
pFastBac HsABRO1	This paper	N/A
pFastBac HsBRCC36	This paper	N/A
pFastBac HsBRE	This paper	N/A
pFastBac HsMERIT40	This paper	N/A
pFastBac SHMT2	This paper	N/A
pFastBac Strep-BirA-HsABRO1	This paper	N/A
SHMT2α	SGC structural genomics consortium	3OU5
GFP-RAP80(WT)	Dr. A.M. Jetten	N/A
GFP-RAP80(ΔAIR) (Δ274-334)	This paper	N/A
pFasBac- mouse ABRO1 (1-260) - ABRAXAS (269-407)	This paper	N/A
Human BRCA1-BRCT	Wu et al., 2016	N/A
pFastBac- ABRAXAS-sortase site -FLAG tag at the C terminus (ABRAXAS 1-394 - LPETGDYKDHDGDYKDHDIDYKDDDDK)	This paper	N/A
Software and Algorithms		
Fiji	Schindelin et al., 2012	https://fiji.sc
DYNAFIT	Kuzmič, 2009	http://www.biokin.com/dynafit/
Prism		https://www.graphpad.com
XDS	Kabsch, 2010	http://xds.mpimf-heidelberg.mpg.de
DIALS	Winter et al., 2018	https://dials.diamond.ac.uk
POINTLESS	Evans, 2011	http://www.ccp4.ac.uk
AIMLESS	Evans and Murshudov, 2013	http://www.ccp4.ac.uk
STARANISO	Global Phasing	http://staraniso.globalphasing.org
SHELXD	Sheldrick, 2008	http://shelx.uni-goettingen.de
PHASER	McCoy et al., 2007	https://www.phaser.cimr.cam.ac.uk/
PIRATE	Cowtan, 2000	http://www.ccp4.ac.uk
PARROT	Cowtan, 2010	http://www.ccp4.ac.uk
PHENIX	Adams et al., 2010	https://www.phenix-online.org
COOT	Emsley et al., 2010	https://www2.mrc-lmb.cam.ac.uk/personal/pemsley/coot/
ISOLDE	Croll, 2018	https://isolde.cimr.cam.ac.uk
REFMAC	Nicholls et al., 2012	http://www.ccp4.ac.uk
AUTOBUSTER	Global Phasing	https://www.globalphasing.com

(*Continued on next page*)

Continued

REAGENT or RESOURCE	SOURCE	IDENTIFIER
CNS	Schröder et al., 2010	http://cns-online.org/v1.3/
ROSETTA	Wang et al., 2016	https://www.rosettacommons.org
PDB-REDO	Joosten et al., 2014	https://pdb-redo.eu
MOLPROBITY	Chen et al., 2010	http://molprobity.biochem.duke.edu
CryoFLARE	A.D.S., unpublished data	http://www.cryoflare.org
motioncor2	Li et al., 2013	https://msg.ucsf.edu/software
GCTF	Zhang, 2016	https://www.mrc-lmb.cam.ac.uk/kzhang/
Gautomatch		https://www.mrc-lmb.cam.ac.uk/kzhang/
RELION	Scheres, 2012	https://www3.mrc-lmb.cam.ac.uk/relion
EMAN2	Tang et al., 2007	https://blake.bcm.edu/emanwiki/
ResMap	Kucukelbir et al., 2014	http://resmap.sourceforge.net

CONTACT FOR REAGENT AND RESOURCE SHARING

Requests for further information, resources, and reagents should be directed to and will be fulfilled by the lead contact Nicolas H. Thomä (nicolas.thoma@fmi.ch).

EXPERIMENTAL MODEL AND SUBJECT DETAILS

Cell culture of human osteosarcoma (U2OS) cells

U2OS cells (female, a gift from Dr. Durocher) were cultured at 37°C in an atmosphere of 5% CO_2 in DMEM supplemented with antibiotics, 10% fetal calf serum and glutaMAX (GIBCO). They were not otherwise authenticated.

METHOD DETAILS

Protein expression and purification of BRCA1-A and BRISC

Expression constructs for the BRCA1-A and BRISC complex were synthesized (Genescript and Geneart, for *Mus musculus* and *Homo sapiens,* respectively) and cloned into pFastBac (ThermoFisher) vectors for insect cell expression using standard molecular biology techniques. Native codon usage was preserved with the exception of the removal of NotI and KpnI restriction sites. Truncated constructs were cloned from full-length constructs using standard molecular biology techniques. All constructs were verified by sequencing (Microsynth). Baculoviruses were generated in *Spodoptera frugiperda* Sf9 cells (ThermoFisher) using the Bac-to-Bac system (ThermoFisher). For recombinant protein expression of the BRCA1-A and BRISC complex or subcomplexes, *Trichoplusia ni* High Five cells (ExpressionSystems) were coinfected with baculoviruses encoding the desired proteins. BRCA1-A complex was expressed by co-infection of High Five cells with viruses encoding (full-length, engineered or truncated) ABRAXAS, BRCC36, BRE, MERIT40, and RAP80. BRISC complex was expressed by co-infection of High Five cells with viruses encoding (full-length, engineered or truncated) ABRO1, BRCC36, BRE, and MERIT40. The BRE-MERIT40 complex was expressed by co-infection of High Five cells with viruses encoding BRE and MERIT40. Cells were harvested by centrifugation 36 h after infection, resuspended in lysis buffer (50 mM HEPES pH 7.4, 200 mM NaCl, 0.1% (v/v) Triton X-100, 1 mM PMSF, 0.2 mM TCEP) supplemented with 1 × SigmaFast protease inhibitor cocktail (Sigma-Aldrich) and disrupted by sonication. Cell debris was removed by ultracentrifugation (45 min at 40,000*g*) and the supernatant was filtrated through Miracloth (EMD Millipore) and subsequently applied to Strep-Tactin resin (IBA Lifesciences). The affinity resin was washed (wash buffer: 50 mM HEPES pH 7.4, 200 mM NaCl, 0.2 mM TCEP) and bound protein was subsequently eluted (elution buffer: 50 mM HEPES pH 7.4, 200 mM NaCl, 0.2 mM TCEP, 2.5 mM D-desthiobiotin). The eluted complex was subjected to anion exchange purification on a Poros 50 HQ (ThermoFisher) column using a linear gradient (50 mM Tris-HCl pH 8.0, 0.2-1 M NaCl, 0.2 mM TCEP). Fractions containing protein were concentrated by ultrafiltration (Amicon Ultra-15, 30 kDa molecular weight cutoff). For crystallization, concentrated BRCA1-A was incubated at room temperature (RT) with 1% (w/w) tobacco etch virus (TEV) protease for 1 h to remove affinity tags. Samples were finally subjected to gel filtration on a Superose 6 column (ThermoFisher), where buffer was exchanged to crystallization buffer (20 mM HEPES pH 7.4, 150 mM NaCl, 0.2 mM TCEP) or storage buffer (50 mM HEPES pH 7.4, 200 mM NaCl, 0.2 mM TCEP).

BRCA1-A crystallization

BRCA1-A (10 mg/ml in crystallization buffer) was crystallized in Cryschem plates (Hampton Research) by vapor diffusion equilibration against 500 μl well solution. Crystallization trials were set up by mixing 1 μl BRCA1-A solution with 1 μl well solution (100 mM

MES-KOH pH 5.6, 200 mM $MgCl_2$, 8% (w/v) PEG6000) at room temperature. The plate was subsequently incubated at 4°C and rhombohedral plate-like crystals grew. They obtained their largest dimension after three days. Crystals were cryoprotected by gradual supplementation of the crystal growth drop with ethylene glycol to a final concentration of 25% (v/v), and flash-cooled in liquid nitrogen for X-ray diffraction analysis.

BRCA1-A crystal structure determination

BRCA1-A formed crystals belonging to the orthorhombic space group $P2_12_12_1$ with unit cell parameters a = 97.1 Å, b = 112.6 Å, c = 431.3 Å, and contained a single copy of the complex, with a molecular weight of 333 kDa in the asymmetric unit and solvent content of ~65%. These crystals typically diffracted X-rays anisotropically to 4.2 Å resolution. All diffraction data were collected at the Swiss Light Source (SLS) from crystals cooled to 100 K as described. In a native zinc single wavelength anomalous dispersion (SAD) phasing approach, high-multiplicity diffraction data were collected from a fixed position on a single crystal with a low-dose X-ray beam at the zinc K-edge absorption peak wavelength (1.2816 Å; $f' = -9.23$, $f'' = 4.97$) from SLS beamline X10SA with a Pilatus 6M detector (Dectris). Data were processed with *XDS* (Kabsch, 2010). Two sites corresponding to the BRCC36 active site Zn^{2+} ions were found using the anomalous intensities in the resolution range 118-7.5 Å with *SHELXD* (Sheldrick, 2008). SAD phases were calculated from the two sites after refinement in *PHASER* (McCoy et al., 2007) to 7.3 Å resolution, giving an overall figure-of-merit of 0.29. Density modification was carried out initially with *PIRATE* (Cowtan, 2000) from the CCP4 suite (Winn et al., 2011) at 7.3 Å resolution and thereafter with *PARROT* (Cowtan, 2010) or *phenix.resolve* (Adams et al., 2010). SAD phasing was reinitiated in *PHASER* using the density modified map as the partial structure (MR-SAD) and followed by a round of density modification to generate an improved electron density map. By iterating this procedure, the phases were progressively extended to 6 Å resolution, yielding substantially improved electron density. The atomic model was built interactively in *COOT* (Emsley et al., 2010). At first domain fragments were placed in the electron density from known structures for the ABRAXAS-BRCC36 MPN domain dimer (PDB: 4d10; Lingaraju et al., 2014), the BRE UEV-C domain (PDB: 4YII; Brown et al., 2015), and MERIT40 (PDB: 2X5N; Riedinger et al., 2010), and ideal α-helices in other regions clearly defined by tubes of electron density. Dramatic improvement to the interpretability of the electron density was achieved through many cycles of poly-serine model building followed by consecutive refinement in *CNS* (Schröder et al., 2010) with non-crystallographic symmetry (NCS) and deformable elastic network restraints (γ = 0 and w_{DEN} = 100), and *REFMAC* (Nicholls et al., 2012) with jelly-body restraints (σ = 0.01 for 100–500 cycles), followed by density modification with NCS averaging. Refinement was carried out using SAD phase restraints against the Zn-SAD data in resolution range 118-4.3 Å, or data to comparable resolution obtained from different crystals. Once the quality of the electron density indicated that completing the atomic model would be feasible, focus was shifted to assigning its amino acid sequence, and increasing consideration was given to the validation characteristics of the refined coordinates. Diffraction data for model completion and refinement were assembled by multi-crystal merging across seven crystals, improving overall data quality and the measurability of reflections in a cone around the a^* (a) axis, which was the weakest direction of anisotropy. Diffraction data were obtained SLS beamline X06SA with an Eiger X 16M detector (Dectris) at a wavelength of 1 Å and processed using *DIALS* (Winter et al., 2018), with diffraction geometry parameters adjusted by joint refinement across multiple sweeps obtained from several crystals. Intensity data were combined with *POINTLESS* (Evans, 2011) and scaled and merged with *AIMLESS* (Evans and Murshudov, 2013). Structure factor amplitudes treated for anisotropy were calculated from the final intensities by *STARANISO* (Global Phasing Ltd.), applying a high-resolution cut-off of 1 $I/\sigma I$. Amino acid sequence assignment was guided by the positions of methionine and cysteine residues determined by MR-SAD for the native sulfur atoms in combination with the mercury atoms found for a crystal soaked in *p*-chloromercuribenzoic acid. The model was rebuilt and extended with *COOT* in cycle with refinement against data extending to 3.75 Å resolution variously with *autoBUSTER* (Global Phasing Ltd.), *phenix.refine*, *ROSETTA* (Wang et al., 2016), and *REFMAC.* Development of the refinement strategy was guided by analysis with *PDB-REDO* (Joosten et al., 2014). Final refinement was performed with *ISOLDE* followed by *REFMAC* (Croll, 2018; Nicholls et al., 2012). Analysis of the final model with *MOLPROBITY* (Chen et al., 2010) indicates that 92.5% of the residues are in favorable regions of the Ramachandran plot, with 1.2% outliers. Detailed crystallographic data processing and refinement statistics are in Table 1.

Protein expression and purification of SHMT2α

The expression construct for SHMT2 encoding the cytosolic form SHMT2α was obtained from the SGC structural genomics consortium and contains a mutation A264T, which is distal from the BRISC interaction surface. In comparison with the PLP-bound SHMT2 structure (PDB: 4PVF) there is no indication that the mutation affects the overall structure (PDB: 6DK3). SHMT2α was expressed at 15°C overnight in *Escherichia coli* BL21 (DE3) pRIL (Agilent Technologies) in auto-induction medium (Studier, 2005). Cells were resuspended in lysis buffer (50 mM HEPES pH 7.4, 200 mM NaCl, 0.1% (v/v) Triton X-100, 1 mM PMSF, 1 × SigmaFast protease inhibitor (Sigma-Aldrich), 0.2 mM TCEP) and lysed by sonication. Cell debris was subsequently removed by ultracentrifugation. The supernatant was subjected to Ni-NTA (Sigma-Aldrich) affinity chromatography. The protein was eluated using steps of 5, 20, 50, 100, 500 mM imidazole (buffer: 100 mM HEPES pH 7.4, 200 mM NaCl, 0.2 mM TCEP) and pooled protein fractions were concentrated by ultrafiltration (Amicon Ultra-15, 30 kDa molecular weight cutoff, Merck) and separated by gel filtration on a Superdex 200 column (ThermoFisher). SHMT2α was purified in its *apo*-form lacking pyridoxal 5′-phosphate (PLP). To assemble SHMT2 tetramers with bound cofactor, PLP (Sigma-Aldrich) was added to SHMT2α prior to gel filtration. The protein fractions obtained showed the characteristic yellow color indicative of PLP binding.

Cryo-electron microscopy

For structure determination of BRISC-SHMT2 complex by cryo-electron microscopy equal volumes of human BRISC (12 mg/ml) and SHMT2 (9.3 mg/ml) were mixed and incubated at room temperature for 15 min. The complex was purified by gel filtration (Superose 6, GE Healthcare) and the peak fraction (0.44 mg/ml) was collected. Tween-20 was added to a final concentration of 0.001% (v/v). Gold foil grids UltrAuFoil 1.2/1.3 300 mesh (Quantifoil) were glow discharged in a Solarus plasma cleaner (Gatan) for 12 s in a H_2/O_2 environment prior to vitrification. A 4 μl sample was applied to the grid and a protocol consisting of 30 s pre-blot incubation, 2 s blotting and no post-blot incubation was utilized for vitrification using a Leica EM GP plunge freezer (Leica Microsystems) operated at 4°C and 80% humidity. Data were collected automatically with EPU (ThermoFisher) on a Cs corrected (CEOS) FEI Titan Krios (ThermoFisher) electron microscope at 300 kV. Zero-energy loss micrographs were recorded using a Gatan K2 summit direct electron detector (Gatan) in counting mode located after a Quantum-LS energy filter operated with a slit width of 20 eV. The acquisition was performed at a calibrated magnification of 58140x in EFTEM mode yielding a pixel size of 0.86 Å and a dose rate of 4.7 $e^-/(px \cdot s)$. Exposures of 7 s were fractionated into 40 frames leading to a total dose of 45 $e^-/Å^2$. The defocus values of the dataset ranged from −0.5 to −5 μm.

Image processing

Parallel to acquisition with EPU the micrograph stacks were corrected for drift, the CTF was determined, and particles were auto picked using *CryoFLARE* (in house development; www.cryoflare.org) for automation of the process. The drift correction was performed with the program motioncor2 (Li et al., 2013). A sum of all 40 frames was generated with and without applying a dose weighting scheme. The CTF was fitted using *GCTF* (Zhang, 2016) on the non-dose-weighted sums and the particles were picked using *Gautomatch* (Dr. Kai Zhang, Cambridge) on the dose-weighted sums. A total of 1822 micrograph movies were acquired from which 332,598 particles were selected. The corrected and picked dataset was subsequently subjected to extraction with a box size of 350 px from the dose-weighted sums and resulting particles were 2D classified. Six rounds of 2D classification in *RELION* (Scheres, 2012) and selection of good classes were performed to remove ice contamination, junk particles, and particles touching each other due to micro-aggregation. The 2D classfication and selection process yielded a refined dataset of 44,381 particles. An initial 3D model was generated in *RELION* without imposing symmetry. The initial model was rotated in chimera to align the twofold symmetry axis of the complex with Z and afterward symmetrized in C2 using *EMAN2* (Tang et al., 2007). The symmetrized map was used as a starting model for a 3D classification into 3 classes in *RELION*. The largest class containing 35,595 particles was selected for 3D refinement. The refined dataset was used to re-extract particles from dose-weighted sums where the first 3 and the last 20 frames were excluded. The re-extracted dataset was subjected to another round of 3D refinement yielding a map at 3.9 Å resolution. The refinements followed the gold-standard procedure and the resolution estimates are based on the Fourier shell correlation curve (FSC) at the 0.143 criterion (Rosenthal and Henderson, 2003) after post-processing. The final map was corrected for the modulation transfer function (MTF) of the K2 detector and sharpened by applying a negative *B* factor estimated automatically within *RELION*. Variations in the local resolution were estimated from the independent half-maps of the refinement using the program *ResMap* (Kucukelbir et al., 2014). Our BRCA1-A atomic model and SHMT2 (PDB: 5V7I, Ducker et al., 2017) were docked into the BRISC-SHMT2α cryo-EM map with *COOT*. Using tools from *ROSETTA* suite and *PROMALS3D* (Pei et al., 2008), the human BRISC amino acid sequence was assigned by threading, the protomer conformations were optimized, and refinement with iterative local rebuilding was carried out. The final model was obtained after minimal cycles of rebuilding with *COOT* and refinement with *phenix.real_space_refine.* Detailed cryo-EM data collection, refinement, and validation statistics are in Table 2.

Chain length specific degradation assay

To assess chain length dependence of human BRISC and BRCA1-A (truncated RAP80) DUB activity, 4 μg K63-linked $(Ub)_2$, $(Ub)_3$, or $(Ub)_4$ (Boston Biochem) were incubated with 5 nM DUB complex in 210 μl volume (gel filtration buffer). Samples (10 μl) were taken at regular intervals, reactions were stopped by addition of SDS-PAGE loading buffer and subsequently samples were analyzed qualitatively by SDS-PAGE (AnyKD, Bio-Rad) and silver stain (Bio-Rad). Initial velocity of cleavage of $(Ub)_2$ at variable BRCA1-A concentrations (0-500 nM) was measured using 200 nM internally quenched K63-linked $(Ub)_2$ as substrate in assay buffer (50 mM HEPES pH 7.0, 100 mM NaCl, 0.5% (w/v) BSA, 0.03% (w/v) Brij-35, 0.2 mM TCEP). Relative TAMRA fluorescence was monitored in 10 s time increments (excitation at 540 nm, emission at 590 nm) and assays were carried out at 22°C in black flat-bottom high-base 386-well plates (Greiner Bio-One) using a Pherastar plate reader (BMG Labtech). Initial velocity in relative fluorescence units per second was determined by linear regression.

Nuclear magnetic resonance experiments

NMR experiments were conducted at 25°C on a Varian INOVA 600-MHz spectrometer equipped with ^1H, ^{13}C, ^{15}N triple-resonance, z axis pulsed-field-gradient probe. All samples were prepared in a buffer 50 mM HEPES pH 7.4, 200 mM NaCl, 0.2 mM TCEP, and 5% D_2O. All NMR data were processed with NMRPipe and NMRDraw (Delaglio et al., 1995). NMR data were obtained from standard 1D single-resonance experiments acquired on 100 μM uniformly ^{15}N–labeled Ubiquitin purchased from BostonBiochem. ^{15}N-HSQC titration of 50 μM ^{15}N-Ubiquitin proteins was done by stepwise addition of MERIT40 truncated, MERIT40 full-length mixed 1:1 with BRE, or Merit40 truncated mixed 1:1 with BRE from high concentration stocks. ^{15}N-HSQC titration data were analyzed with SPARKY (https://www.cgl.ucsf.edu/home/sparky/).

$(Ub)_4$ pre-orientation assay

Human BRCA1-A (containing truncated RAP80) at a concentration of 10 nM was mixed with 1 μM $(Ub)_4$ with a TAMRA label on the proximal (Life Sensors) and distal (Boston Biochem) Ubiquitin, respectively, in assay buffer (50 mM HEPES pH 7.0, 100 mM NaCl, 0.5% (w/v) BSA, 0.03% (w/v) Brij-35, 0.2 mM TCEP). Samples (10 μl) were taken at regular intervals and reactions were stopped by addition of SDS-PAGE loading buffer. Gels were analyzed by SDS-PAGE (AnyKD, Bio-Rad) and imaged with a Typhoon FLA 9500 imager (GE Healtchare Life Sciences).

Cell biology and fluorescence microscopy of DNA repair foci

U2OS parental and RAP80 knockout cells were used. The knockout of RAP80 was confirmed by western blot analysis using RAP80-specific antibody. The GFP-RAP80(WT) plasmid was a gift of Dr. A.M. Jetten (Yan et al., 2002). This plasmid was used to remove the AIR domain (residues 274-334) to generate GFP-RAP80(ΔAIR). Both parental and RAP80 knockout cells were seeded on 18 mm coverslips and transiently transfected with 25 ng GFP-NLS, 500 ng GFP-RAP80(WT) or 500 ng GFP-RAP80(ΔAIR) using lipofectamine 2000 according to the manufacturer's instructions. At 24 h after transfection, cells were irradiated with 2 Gy using a YXlon X-ray generator (YXlon International, 200 KV, 10 mA, dose rate 2 Gy/min) and after 1 h cells were fixed with 4% formaldehyde in PBS for 15 min at room temperature. Cells were treated with 100 mM glycine in PBS for 10 min to block unreacted aldehyde groups. Cells were rinsed with phosphate-buffered saline and equilibrated in WB (PBS containing 0.5% BSA, and 0.05% Tween 20; Sigma-Aldrich). Antibody steps and washes were in WB. The primary antibodies (mouse BRCA1 Santa Cruz sc-6954; 1/100, and rabbit MDC1 Abcam ab11171; 1/1000) were incubated overnight at 4°C. Detection was done using goat anti-mouse or goat anti-rabbit Ig coupled to Alexa 555 or 647 (1/1000; Invitrogen Molecular probes). Samples were incubated with 0.1 μg/ml DAPI and mounted in Polymount. Images of fixed samples were acquired on a Zeiss AxioImager M2 widefield fluorescence microscope equipped with 63x PLAN APO (1.4 NA) oil-immersion objectives (Zeiss) and an HXP 120 metal-halide lamp used for excitation. Fluorescent probes were detected using the following filters: DAPI (excitation filter: 350/50 nm, dichroic mirror: 400 nm, emission filter: 460/50 nm), GFP (excitation filter: 470/40 nm, dichroic mirror: 495 nm, emission filter: 525/50 nm), Alexa 555 (excitation filter: 545/25 nm, dichroic mirror: 565 nm, emission filter: 605/70 nm), and Alexa 647 (excitation filter: 640/30 nm, dichroic mirror: 660 nm, emission filter: 690/50 nm). Images were recorded using ZEN 2012 software. The number, intensity, and size of BRCA1 foci was analyzed for all conditions in ImageJ using a custom-built macro that enabled automatic and objective analysis of the foci as described previously (Typas et al., 2015). Cell extracts were generated by boiling cell pellets in Laemmli buffer, separated by SDS-PAGE and transferred to Immobilon-FL PVDF membranes (Millipore). Membranes were probed with the following antibodies: rabbit anti-RAP80 (Bethyl A300-764, 1/1000), mouse anti-GFP (Roche 11814460001, 1/2000), and mouse anti-tubulin (Sigma T6199, 1/5000). Protein detection was done using the Odyssey infrared imaging scanning system (LI-COR Biosciences). Secondary antibodies were purchased from Biotium.

Co-expression in insect cells and pull-down

High Five cells were grown to $5 \cdot 10^6$ cells/ml and 5 ml were mixed with 5 ml of fresh medium supplemented with penicillin and streptomycin and infected by addition of 200 μl of P2 virus. Cells were harvested after 40 h, pelleted. and lysed by sonication in lysis buffer (50 mM HEPES pH 7.4, 200 mM NaCl, 0.1% Triton X-100, 0.2 mM TCEP). Lysate was cleared by centrifugation (13200 rpm at 30 min, 4°C). 25 μl Ni-NTA (Sigma-Aldrich) or 15 μl Strep-Macro-Prep (IBA AG) were added and sample was incubated on a shaking platform at 4°C for 30 min. After two washes with lysis buffer, the resin was resuspended in SDS-PAGE sample buffer and analyzed by SDS-PAGE.

Analysis of RAP80 incorporation and double arc formation

A fusion gene of mouse ABRO1 (residues 1-260) and ABRAXAS (residues 269-407) was synthesized by IDT and cloned into pFastBac baculovirus expression vector. Fusion complex was prepared as described for BRCA1-A complex, using fusion virus instead of ABRAXAS. Oligomerization was analyzed by SDS-PAGE (AnyKD gels, BioRad) and native PAGE electrophoresis (7.5% (w/v) acrylamide gels, BioRad) using 10 μg of complex for each lane. Gels were stained with Coomassie brilliant blue.

Negative stain electron microscopy

BRISC was prepared for electron microscopy using the GraFix method (Kastner et al., 2008). BRISC complex (10 mg/ml) was layered on top of a 10%–30% (w/v) glycerol gradient (50 mM HEPES pH 7.4, 150 mM NaCl, 0.2 mM TCEP) with an increasing concentration (0%–0.2% w/v) of glutaraldehyde (EMS) and subjected to ultracentrifugation (Beckman SW40Ti rotor, 32000 rpm, 19 h, 4°C). The fraction containing BRISC was directly applied to glow discharged Quantifoil grids (S7/2, Cu 400 mesh, Quantifoil Micro Tools GmbH), blotted, and stained with 2% (w/v) uranyl acetate. Data were collected using a Tecnai T12 electron microscope (FEI) at 100 kV, with a pixel size of 3.08 Å/pixel at the specimen level. Images were recorded with a TVIPS TemCam F416 with varying defocus (−0.5 to −1.5 μm) and processed with the EMAN2 image processing suite (Tang et al., 2007).

Di-ubiquitin preparation

K63-linked di-Ubiquitin (K63-$(Ub)_2$) contains WT Ubiquitin linked by K63 to an N-terminally his-tagged Ubiquitin bearing a K63R mutation. To prepare K63-diUb, 300 μM his-tagged Ubiquitin K63R and 100 μM wild-type (WT) Ubiquitin were incubated with 0.1 μM E1,

2.5 μM Ubc13, 2.5 μM Ube2V2 and 0.55 μM RNF4∼RING at 20°C overnight in a buffer containing 3 mM ATP, 5 mM $MgCl_2$, 50 mM Tris pH 7.5, 150 mM NaCl, 0.5 mM TCEP and 0.1% NP40. RNF4∼RING contains one full-length RNF4 linearly fused to a second RING domain of RNF4 (Plechanovová et al., 2011). The reaction mixture was purified by Ni-NTA chromatography. The Ni-NTA elution contained His-tagged $(Ub)_2$ and His-tagged ubiquitin K63R, which were separated on a HiLoad Superdex 75 16/600 gel filtration column (ThermoFisher) in a buffer containing 50 mM Tris pH 7.5, 150 mM NaCl and 0.5 mM TCEP.

Preparation of SUMO/Ubiquitin mixed chains

SUMO-2-K63-$(Ub)_2$ was prepared using SUMO-2-Ub as a substrate. SUMO-2-Ub contained WT ubiquitin linearly fused to a C-terminally His-tagged SUMO-2 (Bett et al., 2015). A second Ubiquitin bearing a K63R mutation was enzymatically linked to this substrate via K63 to generate SUMO-2-K63-$(Ub)_2$. In the reaction, 300 μM ubiquitin K63R and 100 μM his-tagged SUMO-2-Ub were incubated with 0.1 μM E1, 2.5 μM Ubc13, 2.5 μM and 0.55 μM RNF4∼RING at 20°C overnight in a buffer containing 3 mM ATP, 5 mM $MgCl_2$, 50 mM Tris-HCl pH 7.5, 150 mM NaCl, 0.5 mM TCEP and 0.1% (v/v) NP40. The reaction mixture was purified by Ni-NTA chromatography. The Ni-NTA elution contained his-tagged SUMO-2-K63-$(Ub)_2$ and his-tagged SUMO-2-Ub, which were separated on a HiLoad Superdex 75 16/600 gel filtration column (ThermoFisher) in a buffer containing 50 mM Tris-HCl pH 7.5, 150 mM NaCl and 0.5 mM TCEP. Long K63-linked ubiquitin chains linked to tetra-SUMO were produced with the same method, using tetra-SUMO and WT Ubiquitin. Reaction products were purified by size exclusion chromatography with a Superdex 200 16/200 gel filtration column (ThermoFisher) and fractions containing chains larger than 100 kDa were pooled.

SUMO/Ubiquitin mixed chains degradation assay

Human BRCA1-A including full-length RAP80 (residues 1-719), or truncated RAP80 (residues 250-413) was prepared recombinantly from insect cells. DUB reactions were started by mixing 1:1 BRCA1-A with the substrate (100 nM BRCA1-A was mixed with 2 μM K63-diUb or SUMO-K63-diUb, and 20 nM BRCA1-A was mixed with 400 ng of Ub_n∼ub∼4xSUMO-2). Samples were taken at the time points indicated and immediately mixed with SDS-PAGE sample buffer (62.5 mM Tris-HCl pH 6.8, 2% (w/v) SDS, 25% (v/v) glycerol, 0.05% (v/v) bromophenol blue, 5% (v/v) β-mercaptoethanol) in order to stop the DUB reaction. Samples were analyzed by SDS-PAGE (Any kD Mini-PROTEAN TGX Precast Protein Gel, Bio-Rad Laboratories) and subsequently visualized by staining with SYPRO Ruby (Sigma-Aldrich). Stained gels were imaged with a Typhoon FLA 9500 imager (GE Healthcare Life Sciences). Band densitometry was performed with Fiji (Schneider et al., 2012).

Protein expression and purification of BRCA1-BRCT

Qian Wu and Tom Blundell kindly provided the expression construct for the human BRCA1-BRCT domain (Wu et al., 2016). BRCA1-BRCT was expressed recombinantly in *E. coli* BL21-CodonPlus (DE3)-RIL cells (Agilent Technologies). Cell pellets were resuspended in lysis buffer containing 50 mM Tris-HCl pH 8.0, 200 mM NaCl, 0.1% Triton X-100, 1 mM PMSF, 0.2 mM TCEP and Roche EDTA-free protease inhibitor (1 tablet per 500 ml) and lysed by sonication. After removal of cell debris by ultracentrifugation (45 min at 40,000*g*), the supernatant was filtrated through Miracloth (EMD Millipore) and subsequently applied to Ni-NTA resin equilibrated with lysis buffer in a gravity flow column. The Ni-NTA resin was washed with wash buffer (50 mM Tris-HCl pH 8.0, 200 mM NaCl, 0.2 mM TCEP) and bound protein was eluted by step gradient using wash buffer supplemented with 10, 50, 200 and 500 mM imidazole, respectively. The eluate was concentrated by ultrafiltration (Amicon Ultra-15, 10 kDa molecular weight cutoff). Gel filtration with a Superdex 75 was used to purify the protein and exchange the buffer to 50 mM Tris-HCl pH 8.0, 150 mM NaCl, 0.2 mM TCEP.

Sortase ligation of phosphorylated peptides to BRCA1-A

Phosphorylated versions of peptides from the C-terminal region of the BRCA1-A subunit ABRAXAS were covalently ligated to BRCA1-A complex using the sortase ligation technique (Guimaraes et al., 2013). A modified human ABRAXAS expression construct was designed adding a sortase recognition site followed by a FLAG tag at the C terminus (replacing the residues C-terminal of residue I394 with the sequence LPETGDYKDHDGDYKDHDIDYKDDDDK). The FLAG tag allowed removal of unlabeled protein by affinity chromatography and detection of successful labeling by SDS-PAGE (3.1 kDa decrease in protein mass). The modified human ABRAXAS expression construct was synthesized (Integrated DNA Technologies) and cloned into a pFastBac expression vector. BRCA1-A containing sortase-tagged ABRAXAS was expressed in insect cells and purified. Synthetic phosphorylated peptides p-Ser404 (GGGFGEYpSRSPTF), p-Ser406 (GGGFGEYSRpSPTF) and p-Ser404/406 (GGGFGEYpSRpSPTF) (Biomatik) were dissolved in peptide buffer (20 mM Tris-HCl pH 8.0, 150 mM NaCl, 5 mM DTT) at 10 mg/ml and adjusted to pH 8.0. For sortase labeling, a final concentration of 8.5 μM BRCA1-A in 50 mM HEPES pH 7.4, 200 mM NaCl, 0.2 mM TCEP), 870 μM peptide in peptide buffer, and 20 μM sortase in 50 mM Tris-HCl, 200 mM NaCl, 10% (v/v) glycerol) were mixed to a final volume of 500 μl. Reactions were incubated at 22°C and monitored for FLAG tag removal by SDS-PAGE analysis; reactions completed within 6 h. Sortase and excess peptide were removed by gel filtration (Superose 6, ThermoFisher) in gel filtration buffer (50 mM HEPES pH 7.4, 150 mM NaCl, 0.2 mM TCEP). Binding of BRCT to phosphorylated BRCA1-A was assessed by band shift in Coomassie Brilliant Blue-stained native PAGE (7.5% Mini-PROTEAN TGX precast protein gel, Bio-Rad Laboratories).

Microscale thermophoresis binding assays

BRCA1-BRCT was labeled with the amine reactive RED-NHS labeling kit (NanoTemper Technologies). The labeled protein was purified by gel filtration over a Superdex 75 column (ThermoFisher) and diluted to 40 nM with assay buffer (50 mM HEPES pH 7.0, 100 mM NaCl, 0.5% BSA, 0.03% Brij-35, 0.2 mM TCEP). To determine the affinity of BRCA1-A p-Ser404/406 for BRCA1-BRCT, BRCA1-A p-Ser404/406 at concentrations between 0 nM and 853 nM was mixed with 20 nM BRCA1-BRCT and non-labeled BRCT in concentrations of 0 nM, 100 nM, 200 nM, 500 nM, 1000 nM was added to replicates. After 10 min incubation at RT, samples were loaded into Monolith NT.115 Premium capillaries (NanoTemper Technologies) and microscale thermophoresis was measured using a Monolith NT.115 (NanoTemper Technologies). For the back-titration, 0-46.6 μM unlabeled BRCA1-BRCT was titrated into 200 nM BRCA1-A p-Ser404/406 and 20 nM labeled BRCA1-BRCT. Affinities were determined by global fit using *DYNAFIT* (Kuzmič, 2009).

Crosslinking mass spectrometry

The approximate position of BRCA1-BRCT in the BRCA1-A-BRCA1-BRCT complex was determined by crosslinking mass spectrometry of BRCA1-A p-Ser404/406 with BRCA1-BRCT.50 μg of BRCA1-A p-Ser404/406 was mixed with 20 μg BRCA1-BRCT in a total volume of 117 μl. A 1 mg aliquot of the CID-cleavable DSSO crosslinking reagent (disuccinimidyl sulfoxide, MW = 388.35, Spacer Arm = 10.3 Å) was brought to room temperature and dissolved in 25 μl of anhydrous DMSO (100 mM stock). First the sample buffer was transferred into a 100 kDa Amicon Ultra spin filter reactor (0.5 ml), followed by protein stock solution. Finally, the crosslinking reagent was added and incubated at room temperature for 1 h. Excess of unreacted reagent was quenched by addition of 2.5 μl of 1M Tris (50 mM final conc.). After 50 min, filters were centrifuged for 2 min at 14000 g to remove crosslinking reagent and non-crosslinked protein. Filters were topped off with 400 μl (max 450 μl) of 8 M urea in 50 mM HEPES pH 8.5 for denaturing and washing, and then centrifuged for 2 min at 14000 g. This step was repeated twice. At the end of each spin, the sample was concentrated to 40-50 μl. The sample was reduced and alkylated by addition of 5.5 μl of reduction/alkylation solution (stock: 50 mM TCEP, 100 mM 2-chloroacetamide, final concentration 5 mM TCEP and 10 mM 2-chloroacetamide) and subsequent incubation for 30 min in the dark. The samples were centrifuged for 2 min at 14000 g and topped-off with 50 mM HEPES pH 8.5, 8M urea, centrifuged 2 min at 14000 *g*. This procedure was repeated twice for washing. The sample was digested by addition of 0.5 μg Lys-C (5 μl of 0.1 μg/μl stock, 1:100 enzyme to protein ratio) and incubation for 4 h at room temperature. The Lys-C digest was diluted 4-fold by addition of 240 μl of 50 μl HEPES pH 8.5 followed by addition of 0.5 μg of trypsin (2.5 μl of 0.2 μg/μl stock, 1:100 enzyme to protein ratio) and digestion overnight. Next, the sample was incubated for four h after addition of an additional aliquot of 0.5 μg of trypsin (1:100) and 35 μl of acetonitrile to a final concentration of 10%. The filter containing the trypsin digest was inverted and spun 1 min at 1000 g to collect the digest into a fresh Eppendorf tube. The digest was acidified with TFA to 1% final concentration, then sonicated, and centrifuged for 5 min at 20000 g. LC-MS analysis was performed using a 2 cm trapping column and a 50 cm analytical column coupled to an Orbitrap Fusion LUMOS mass spectrometer using a 90 h gradient and the MS2_MS3 method.

Bio-layer interferometry

Affinity between BRISC and SHMT2 was measured by bio-layer interferometry with BRISC immobilized on the sensor and SHMT2 in solution. BRISC was expressed with a Strep-BirA tag fused to the N terminus of ABRO1. The reaction mixture of 1 ml BirA-BRISC (4.6 mg/ml), 60 μl BirA enzyme (2.4 mg/ml), 20 μl 1 M $MgCl_2$, 200 μl 2 mM biotin, 100 μl 400 mM ATP pH 7.5 was adjusted to a final volume of 1.5 ml by addition of 620 μl phosphate buffered saline (PBS), incubated at RT for 1 h, and subsequently at 4°C overnight. Biotinylated BRISC complex was purified by gel filtration (Superdex 200, ThermoFisher). Association and dissociation constants were measured in BLI buffer (50 mM HEPES pH 7.4, 100 mM NaCl, 0.2 mM TECP, 2mg/ml BSA) with a BLItz bio-layer interferometer using Streptavidin-coated sensors (FortéBio).

Internally quenched fluorophore (IQF) deubiquitination assays

Cleavage of K63-diUb was measured using an internally quenched $(Ub)_2$ substrate, which carries a fluorophore (TAMRA) on one ubiquitin molecule and a quencher on the other. Following DUB cleavage of the K63 isopeptide bond, a quencher-bound ubiquitin is released and TAMRA fluorescence increases. BRISC activity was tested against six available fluorophore/quencher positions (DU0102, LifeSensors) and compared to cleavage of unlabeled $(Ub)_2$ in a gel-based assay. Subsequent DUB activity assays were performed with linkage type 1 substrate (DU6301, LifeSensors). The deubiquitination reactions were initiated by mixing 5 μl of protein in storage buffer (50 mM HEPES pH 7.4, 200 mM NaCl, 0.2 mM TCEP) with 5 μl of substrate at 400 nM (200 nM final concentration) in assay buffer (50 mM HEPES pH 7.0, 100 mM NaCl, 0.5% BSA, 0.03% Brij-35, 0.2 mM TCEP). Fluorescence was monitored in 10 s time increments (excitation at 540 nm, emission at 590 nm) and molar reaction rates were determined by comparison to TAMRA-ubiquitin (SI270T, LifeSensors) controls. Assays were carried out at 22°C in black flat-bottom high-base 386-well plates (Greiner Bio-One) using a Pherastar plate reader (BMG Labtech). Reaction progress data were fitted globally with *DYNAFIT* (Kuzmič, 2009).

Quantitative fluorescence microscopy of ABRO1 and SHMT2

HEK293T cells were grown in DMEM supplemented with 10% (v/v) FBS on glass coverslips in six-well dishes for 48 h. For mitochondrial labeling, 100 nM MitoTracker Red CMXRos (ThermoFisher) was added to media and cells were incubated for 30 min at 37°C. Cells were washed once in PBS and fixed for 10 min at RT with 4% PFA in PBS. Cells were washed twice with PBS and plasma

membranes were then labeled with 5 μg/ml Alexa Fluor 633-conjugated wheat germ agglutinin (ThermoFisher) for 10 min at RT. Cells were subsequently washed three times with PBS, permeabilized for 15 min at RT in PBS supplemented with 0.2% (v/v) Triton X-100, then blocked for 1 h in PBS supplemented with 10% (v/v) donkey serum and 2% (w/v) BSA. Samples were incubated overnight at 4°C in a humid chamber with primary antibodies diluted in blocking solution (Rabbit anti-SHMT2 (SAB1100388, Sigma-Aldrich, 1:200); Rabbit anti-ABRO1 (ab74333, abcam, 1:100). Samples were washed in PBS then incubated overnight at 4°C with an Alexa Fluor 488-conjugated donkey anti-rabbit antibody (Sigma-Aldrich, 1:500). Samples were washed with PBS and mounted with VectorShield with DAPI (VectorLabs) and sealed with nail polish. Slides were imaged with a W1 Spinning-Disk (Yokogawa) mounted on an Axio Imager Z2 microscope (Zeiss) and controlled with *VISIVIEW* (Visitron). Fluorescence quantification in the different cell compartments was carried out with *FIJI* (Schindelin et al., 2012) on 3D Z stacks as follows: signal was smoothed with a Gaussian filter in all channels; masks for the nuclei and the mitochondria were generated using the DAPI and MitoTracker channels respectively, applying auto-threshold with the Otsu or Moments methods after background subtraction (rolling ball). The same treatment was applied to the Alexa Fluor 488 channel and the resulting image was combined with the masks for nuclei and mitochondria to create a mask for the whole cell; these three masks were then used to quantify in each plane the amount of fluorescence in the Alexa Fluor 488 channel (SHMT2 or ABRO1 staining).

QUANTIFICATION AND STATISTICAL ANALYSIS

Assays were conducted at least in triplicate, with SD reported, with the exception of experiments that were conducted as dilution replicates and fitted globally. Sample size was not determined *a priori*.

DATA AND SOFTWARE AVAILABILITY

The accession number for the crystal structure of BRCA1-A reported in this paper is PDB: 6GVW. The accession number for the cryo-EM density map of BRISC-SHMT2α complex reported in this paper is EMDB: EMDB-0132. The accession number for the model of BRISC-SHMT2α complex reported in this paper is PDB: 6H3C. The link for access to raw imaging data reported in this paper is Mendeley Data: https://dx.doi.org/10.17632/8ntswhp8d5.1.

Molecular Cell, Volume *75*

Supplemental Information

Structural Basis of BRCC36 Function in DNA Repair and Immune Regulation

Julius Rabl, Richard D. Bunker, Andreas D. Schenk, Simone Cavadini, Mark E. Gill, Wassim Abdulrahman, Amparo Andrés-Pons, Martijn S. Luijsterburg, Adel F.M. Ibrahim, Emma Branigan, Jacob D. Aguirre, Aimee H. Marceau, Claire Guérillon, Tewis Bouwmeester, Ulrich Hassiepen, Antoine H.F.M. Peters, Martin Renatus, Laurent Gelman, Seth M. Rubin, Niels Mailand, Haico van Attikum, Ronald T. Hay, and Nicolas H. Thomä

A

protein	alternative names	entrez	length	Da
ABRAXAS	ABRA1, ABRX1, CCDC98, FAM175A	84142	409	46663
ABRO1	ABRX2, KIAA0157, FAM175B	23172	415	46901
BRCA1	BRCAI, BRCC1, BROVCA1, IRIS, FANCS, PNCA4, PPP1R53, PSCP, RNF53	672	1863	207721
BRCC36	BRCC3, C6.1A, CXorf53	79184	316	36072
BRE	BABAM2, BRCC4, BRCC45	9577	383	43552
MERIT40	BABAM1, C19orf62, HSPC142, NBA1	29086	329	36560
RAP80	UIMC1, RXRIP110, X2HRIP110	51720	719	79727
SHMT2	GLY A+, GLYA, GLYM, HEL-S-51e	6472	504	55993

B

```
SP|Q6UWZ7|ABRX1_HUMAN MEGESTSAVLSGFVLGALAFQHLNTDSDTEGFLLGEVKGEAKNSITDSQMDDVEVVYTID 60
SP|Q15018|ABRX2_HUMAN -----MAASISGYTFSAVCFHSANSNADHEGFLLGEVRQEETFSISDSQISNTEFLQVIE 55
                        :* :**:.:.*:.*:  *:::* ********: * . **:***:.:.*.: .*:

SP|Q6UWZ7|ABRX1_HUMAN IQKYIPCYQLFSFYNSSGEVNEQALKKILSNVKKNVVGWYKFRRHSDQIMTFRERLLHKN 120
SP|Q15018|ABRX2_HUMAN IHNHQPCSKLFSFYDYASKVNEESLDRILKDRRKKVIGWYRFRRNTQQQMSYREQVLHKQ 115
                        *::: ** :*****: :.:***::*.:**.: :*:*:***:******:* *::**::***:

SP|Q6UWZ7|ABRX1_HUMAN LQEHFSNQDLVFLLLTPSIITESCSTHRLEHSLYKPQKGLFHRVPLVVANLGMSEQLGYK 180
SP|Q15018|ABRX2_HUMAN LTRILGVPDLVFLLFS-FISTANNSTHALEYVLFRPNRRYNQRISLAIPNLGNTSQQEYK 174
                        * . :.  ******::  * * . *** **: *::*::   :*: *.: *** :.*  **

SP|Q6UWZ7|ABRX1_HUMAN TVSGSCMSTGFSRAVQTHSSKFFEEDGSLKEVHKINEMYASLQEELKSICKKVEDSEQAV 240
SP|Q15018|ABRX2_HUMAN VSSVPNTSQSYAKVIKEHGTDFFDKDGVMKDIRAIYQVYNALQEKVQAVCADVEKSERVV 234
                        . *    * .:::.:: *.:.**::** :*::: * ::* :***::::* .**.**:.*

SP|Q6UWZ7|ABRX1_HUMAN DKLVKDVNRLKREIEKRRGAQIQAAREKNIQKDP-QENIFLCQALRTFFPNSEFLHSCVM 299
SP|Q15018|ABRX2_HUMAN ESCQAEVNKLRRQITQRKNEKEQERRLQQAVLSRQMPSESLDPAFSPRMPSSGFAAEGRS 294
                        :.   :**:*:*:* :*:. : *  * ::   .    .  *  *:   :*.* *  .

SP|Q6UWZ7|ABRX1_HUMAN SLKNRHVSKSSCNYNHHLDVVDNLTLMVEHTDIPEASPASTPQIIKHKALD-LDDRWQFK 358
SP|Q15018|ABRX2_HUMAN TLGDAEASDPPPPYSDFHPNNQES--TLSHSRMERSVFMPRPQAVGSSNYASTSAGLKYP 352
                        :* : ..*.    *...    ::    :.*: : .:     ** :  .     .   ::

SP|Q6UWZ7|ABRX1_HUMAN RSRLLDTQDKRSKADTGSSNQD--------------------KASKMSSPETDEEIEKM 397
SP|Q15018|ABRX2_HUMAN GSGADLPPPQRAAGDSGEDSDDSDYENLIDPTEPSNSEYSHSKDSRPMAHPDEDPRNTQT 412
                         *       :*: .*:*...:*                    .:  *: *: * .  :

SP|Q6UWZ7|ABRX1_HUMAN KGFGEYSRSPTF 409
SP|Q15018|ABRX2_HUMAN SQI--------- 415
                        . :
```

C

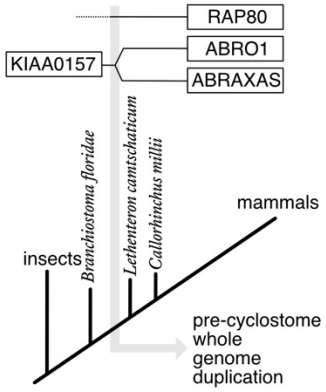

D

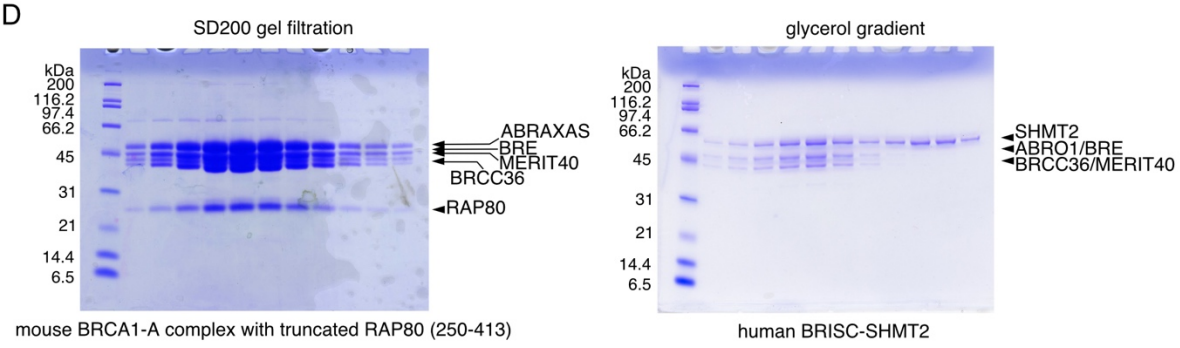

mouse BRCA1-A complex with truncated RAP80 (250-413)

human BRISC-SHMT2

Figure S1. Overview of protein subunits of the BRCA1-A and BRISC complexes, Related to Figure 1

(A) Protein subunits of BRCA1-A and BRISC.

(B) Protein sequence alignment of human ABRAXAS and ABRO1.

(C) Schematic representation of the evolutionary origin of ABRAXAS and ABRO1. Up to and including the lancelet *Branchiostoma floridae* (GCA_000003815.1) animals contain only a single ancestral precursor to ABRAXAS and ABRO1, KIAA0157, and no RAP80. The arctic lamprey *Lethenteron camtschaticum* (GCA_000466285.1) and elephant shark *Callorhinchus milii* (GCA_000165045.2) genomes already contain the two homologs, ABRAXAS and ABRO1, and RAP80, suggesting that they arose during the whole genome duplication preceding the development of cyclostomes (Putnam et al., 2008).

(D) SDS-PAGE analysis of mouse BRCA1-A complex size exclusion chromatography fractions used for crystallization and of human BRISC-SHMT2α complex glycerol gradient fractions (higher to lower density) used for cryo-EM structure determination.

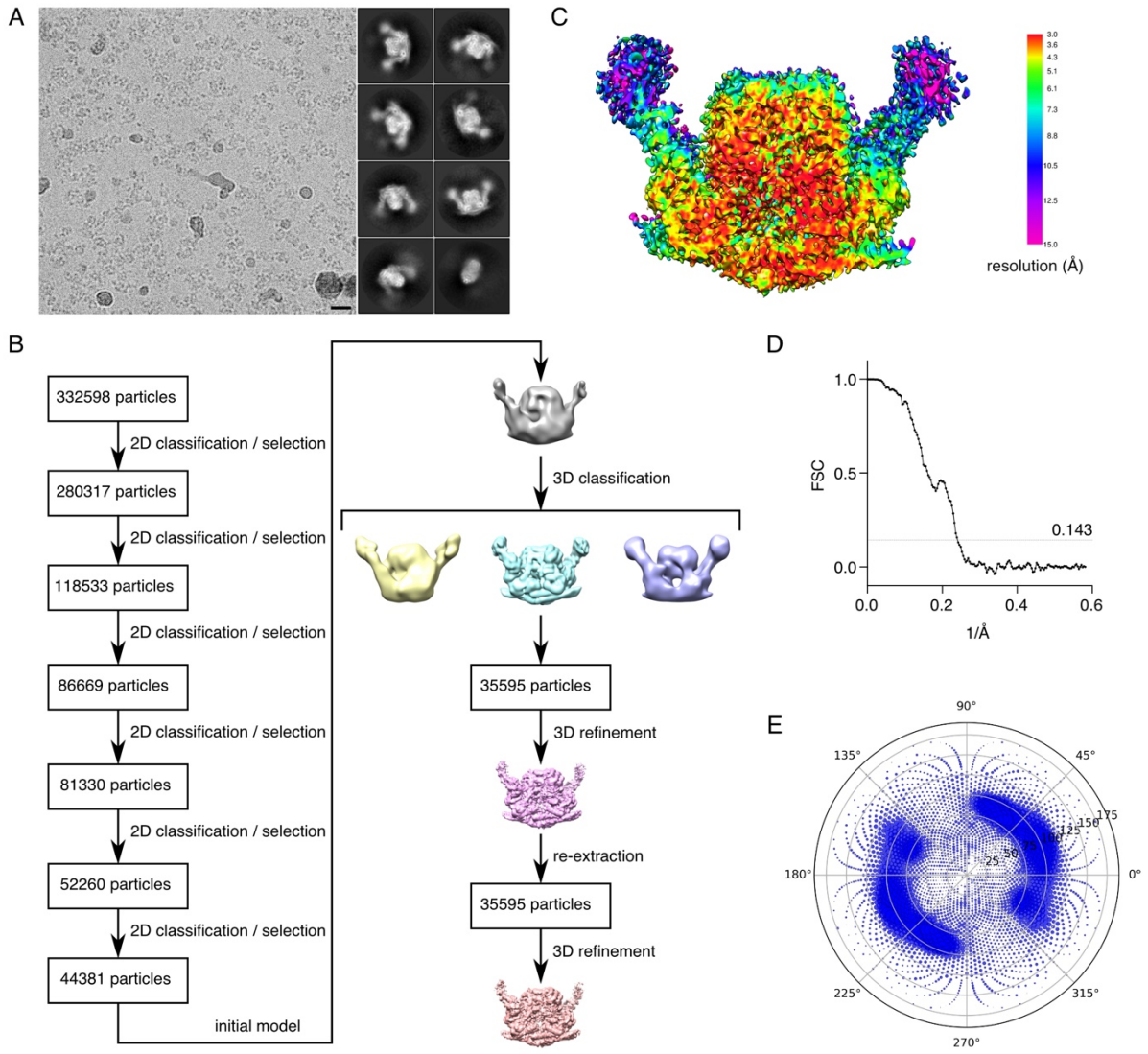

Figure S2. Cryo-EM classification and refinement procedures for BRISC-SHMT2α complex, Related to Figure 1

(A) Representative micrograph (scale bar: 300 Å) and reference-free class averages.

(B) Flowchart representation of data processing strategy.

(D) Gold-standard Fourier shell correlation (FSC) curve.

(E) Angular distribution of particles.

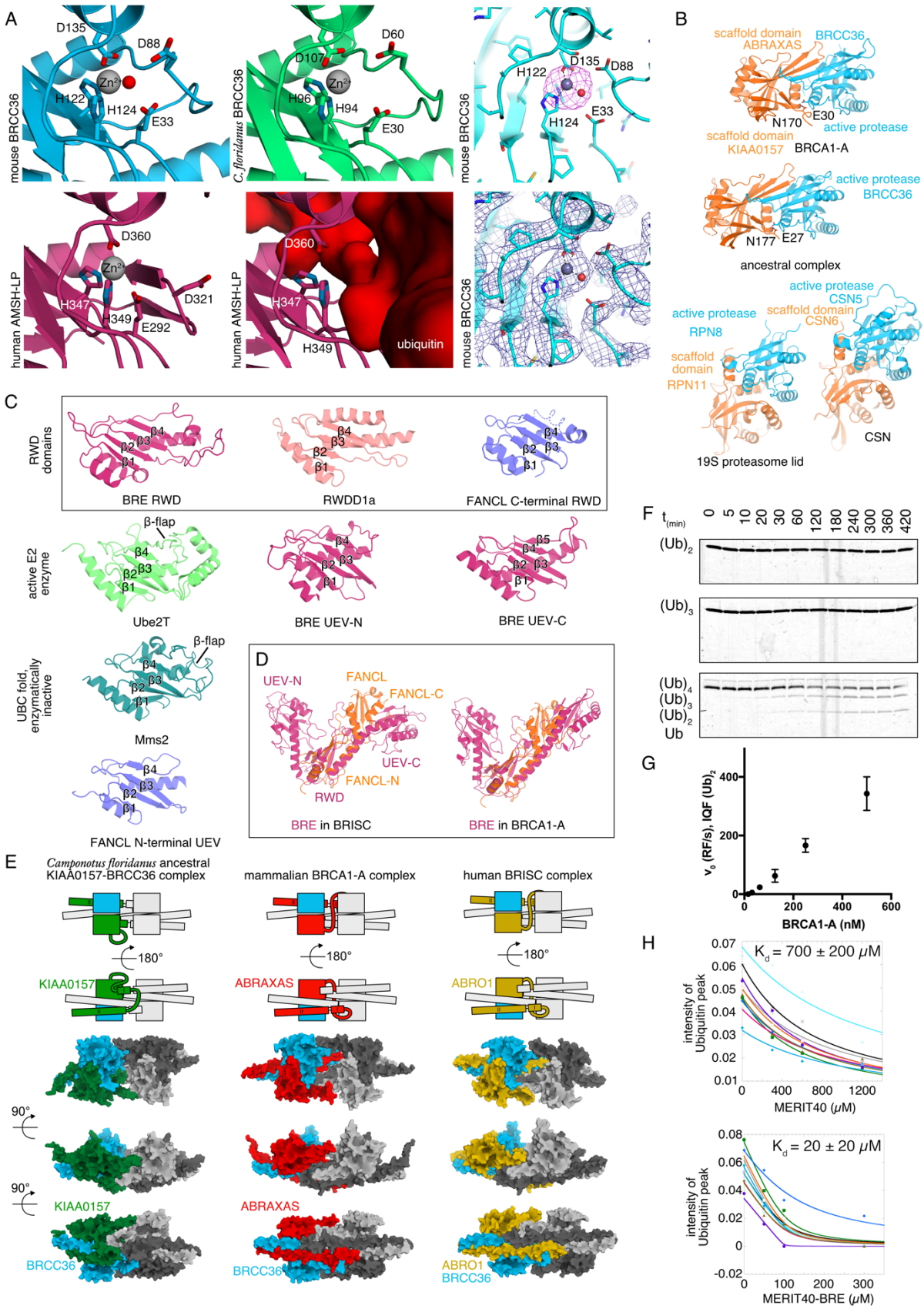
A
mouse BRCC36
D135
D88
H122
H124
E33
C. floridanus BRCC36
D60
D107
H96
H94
E30
mouse BRCC36
H122
D135
D88
H124
E33
human AMSH-LP
D360
H347
H349
E292
D321
human AMSH-LP
D360
H347
H349
ubiquitin
mouse BRCC36
B
scaffold domain
ABRAXAS
BRCC36
N170
E30
active protease
scaffold domain
KIAA0157
BRCA1-A
active protease
BRCC36
N177
E27
ancestral complex
active protease
CSN5
active protease
scaffold domain
CSN6
RPN8
scaffold
domain
RPN11
CSN
19S proteasome lid
C
RWD domains
β1
β2
β3
β4
BRE RWD
RWDD1a
FANCL C-terminal RWD
active E2 enzyme
β-flap
Ube2T
BRE UEV-N
β5
BRE UEV-C
UBC fold, enzymatically inactive
Mms2
FANCL N-terminal UEV
D
UEV-N
FANCL
FANCL-C
UEV-C
FANCL-N
RWD
BRE in BRISC
BRE in BRCA1-A
E
Camponotus floridanus ancestral KIAA0157-BRCC36 complex
mammalian BRCA1-A complex
human BRISC complex
180°
KIAA0157
ABRAXAS
ABRO1
90°
90°
KIAA0157
BRCC36
ABRAXAS
BRCC36
ABRO1
BRCC36
F
t(min)
0
5
10
20
30
60
120
180
240
300
360
420
(Ub)2
(Ub)3
(Ub)4
(Ub)3
(Ub)2
Ub
G
v0 (RF/s), IQF (Ub)2
400
200
0
0
200
400
600
BRCA1-A (nM)
H
Kd = 700 ± 200 μM
intensity of Ubiquitin peak
0.07
0.06
0.05
0.04
0.03
0.02
0.01
0
400
800
1200
MERIT40 (μM)
Kd = 20 ± 20 μM
intensity of Ubiquitin peak
0.08
0.06
0.04
0.02
0
-0.02
0
100
200
300
MERIT40-BRE (μM)

Figure S3. Assembly of BRCA1-A and BRISC and functional aspects. Related to Figures 1 and 2

(A) Cartoon representation of mouse BRCC36 (cyan, top left panel) active site. Residues His122, His124, and Asp135, which coordinate the active site zinc atom, and activation residue Glu33, which coordinates water in the active enzyme are highlighted. Asp88, which lies on Ins-1 adjacent to the active site, is shown. The structure of the mouse BRCC36 active site in context of the assembled complex is highly similar to the structure of ant BRCC36 in the BRCC36-KIAA0157 super-dimer (green, top center panel). Comparison to human AMSH-LP (purple, bottom left panel) shows a highly similar active site. The acidic residue Asp321 on the Ins-1 loop of AMSH-LP, which occludes access to the active site, is conserved between BRCC36 and AMSH-LP, and relocates outward upon di-ubiquitin binding (bottom center panel), suggesting a similar mechanism for BRCC36. Close-up of the BRCC36 active site in BRCA1-A showing the protein in cartoon mode (cyan) with side chains shown as sticks and active site residues labelled overlayed with an anomalous log-likelihood gain map segment showing the prominent peak for the Zn^{2+} ion (gray sphere) calculated with *REFMAC* from an intermediate data set and incomplete model is shown mesh (magenta) and contoured at 7.5 rms (top right panel). The same view as above with a segment of final $2mF_o$-DF_c map calculated by *REFMAC* with regularized negative B-factor sharpening (-160 $Å^2$) shown as mesh (blue) at a contour level of 1 rms and displayed at a radius of 15 Å about the Zn^{2+} ion (bottom right panel).

(B) Interaction between the MPN domain of the active protease and the activating MPN scaffold domain are conserved between the ancestral complex containing KIAA0157 and BRCA1-A containing ABRAXAS (and BRISC; not shown). The arrangement in BRCA1-A differs from what is observed in the 19S proteasome lid and CSN complex. Activation of BRCC36 in BRCA1-A is effected by the interaction between Asn170 of the scaffold subunit ABRAXAS with Glu30 of the activation loop of BRCC36 (residues shown as red spheres). This mechanism is found in the ancestral complex and conserved in BRISC, but sterically not possible in CSN and the proteasome lid.

(C) Structural comparison between the structures of the three UBC fold domains of BRE with the active E2 enzyme, an inactive UBC domain, an RWD domain, and the UEV and RWD domains of human FANCL suggest that the central domain of BRE adopts an RWD fold characterized by a long β-sheet 4 directly followed by an α-helical element.

(D) Alignment of human FANCL and BRE shows that the angle between the UEV and RWD domains of FANCL is similar to the extended conformation observed in the BRE RWD and UEV-C domain.

(E) The position of the linker that connects the MPN domain of the scaffold subunit to the long, C-terminal helix II mediating dimerization differs between the ancestral KIAA0157/BRCC36 complex and the mammalian BRCA1-A and BRISC complexes. A schematic depiction follows the linker from the MPN domain to helix II. Unlike in the ancestral complex where the KIAA0157 (green) linker is positioned along the outer surface of the MPN domain, the ABRAXAS (red) linker crosses on top of the helical bundle and effectively cross-links the super-dimer in the mammalian BRCA1-A complex. In BRISC the ABRO1 (yellow) linker takes a path identical to what is observed in BRCA1-A.

(F) BRISC complex processes $(Ub)_4$ faster than $(Ub)_3$ and $(Ub)_2$. K63-linked ubiquitin substrate (150ng/lane) is incubated with 5 nM BRISC on ice and analyzed by silver stained SDS-PAGE. Under these conditions, $(Ub)_4$ is cleaved within 5 minutes, while $(Ub)_2$ and $(Ub)_3$ are not cleaved within 7 hours.

(G) BRCA1-A is able to efficiently cleave di-Ubiquitin at higher temperature and enzyme concentration. Enzyme titration of BRCA1-A degrading 200 nM internally quenched K63-linked di-Ubiquitin shows increasing v_0 (in relative fluorescence units per second) with increasing enzyme concentration. Error bars represent mean ± SD of n = 3 replicates. Since no saturation was observed using practical concentrations of fluorescent substrate, we were not able to determine the kinetic parameters.

(H) MERIT40 and the MERIT40-BRE complex bind ubiquitin. NMR binding assay by titration of MERIT40 or MERIT40-BRE into ^{15}N-labeled ubiquitin. Peak intensity for ten representative peaks in the HSQC spectrum were measured and plotted as a function of MERIT40 concentration in the titration. Peak intensity diminished as the peaks broadened from the larger molecular weight complex that is formed and/or intermediate exchange. Data were fit to a one-site binding model assuming the bound state has zero peak intensity. The reported K_d is the average affinity over tracking the ten peaks with the standard deviation reported as error.

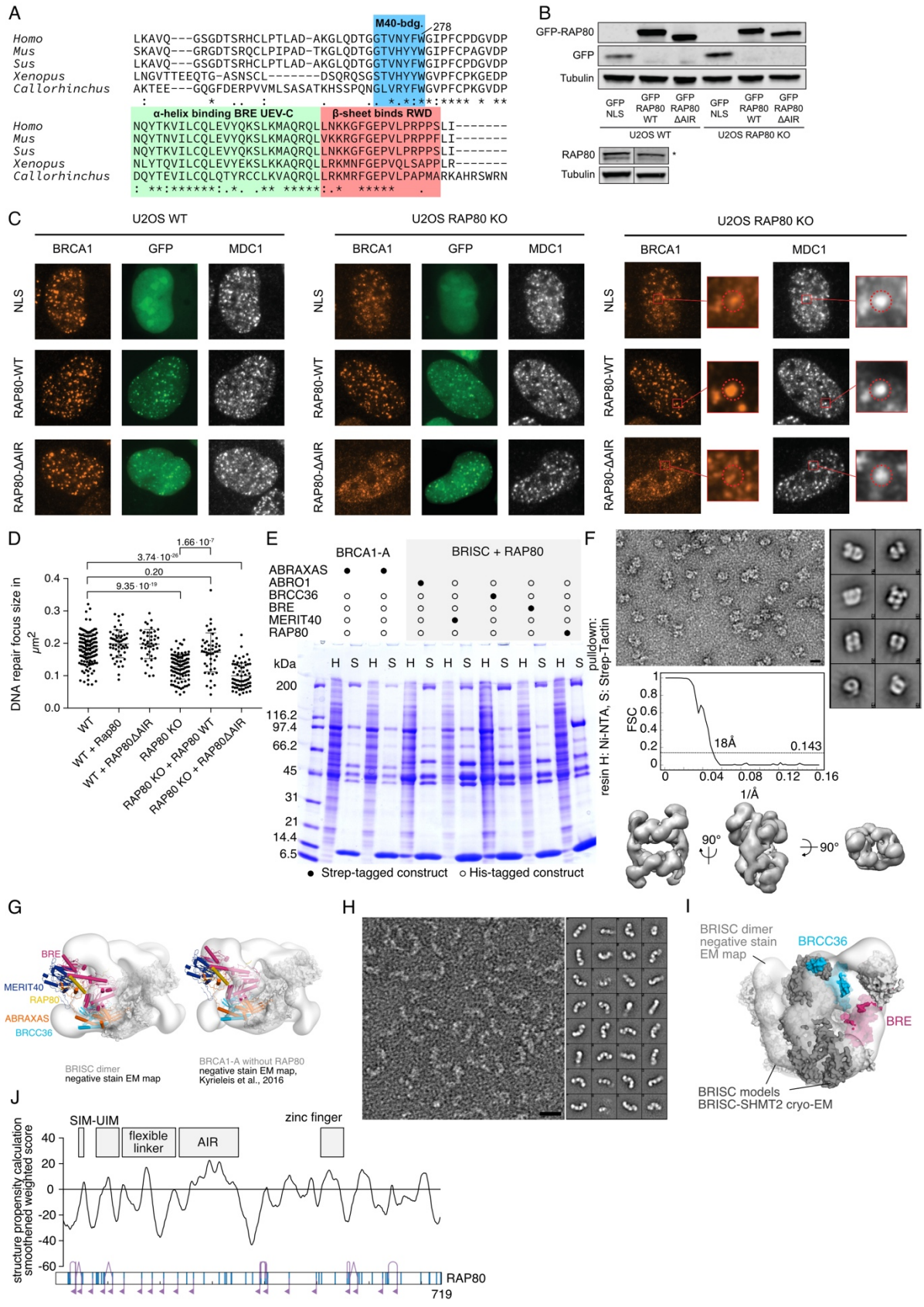
A
M40-bdg.
278
Homo LKAVQ---GSGDTSRHCLPTLAD-AKGLQDTGGTVNYFWGIPFCPDGVDP
Mus SKAVQ---GRGDTSRQCLPIPAD-TKGLQDTGGTVHYYWGIPFCPAGVDP
Sus LKAVQ---GSGDTSRHCLPTLAD-AKGLQDTGGTVNYFWGIPFCPDGVDP
Xenopus LNGVTTEEQTG-ASNSCL-------DSQRQSGSTVHYYWGVPFCPKGEDP
Callorhinchus AKTEE---GQGFDERPVVMLSASATKHSSPQNGLVRYFWGVPFCPKGVDP
α-helix binding BRE UEV-C
β-sheet binds RWD
Homo NQYTKVILCQLEVYQKSLKMAQRQLLNKKGFGEPVLPRPPSLI-------
Mus NQYTNVILCQLEVYQKSLKMAQRQLVKKRGFGEPVLPRPPFLI-------
Sus NQYTKVILCQLEVYQKSLKMAQRQLLNKKGFGEPVLPRPPSLI-------
Xenopus NLYTQVILCQLEVYEKSLKKAQRQLLRKMNFGEPVQLSAPPLR-------
Callorhinchus DQYTEVILCQLQTYRCCLKVAQRQLLRKMRFGEPVLPAPMARKAHRSWRN
B
GFP-RAP80
GFP
Tubulin
GFP NLS
GFP RAP80 WT
GFP RAP80 ΔAIR
GFP NLS
GFP RAP80 WT
GFP RAP80 ΔAIR
U2OS WT
U2OS RAP80 KO
RAP80
Tubulin
C
U2OS WT
U2OS RAP80 KO
U2OS RAP80 KO
BRCA1
GFP
MDC1
NLS
RAP80-WT
RAP80-ΔAIR
D
DNA repair focus size in μm²
1.66·10⁻⁷
3.74·10⁻²⁶
0.20
9.35·10⁻¹⁹
WT
WT + Rap80
WT + RAP80ΔAIR
RAP80 KO
RAP80 KO + RAP80 WT
RAP80 KO + RAP80ΔAIR
E
BRCA1-A
BRISC + RAP80
ABRAXAS
ABRO1
BRCC36
BRE
MERIT40
RAP80
kDa
H S H S H S H S H S H S H S
200
116.2
97.4
66.2
45
31
21
14.4
6.5
Strep-tagged construct
His-tagged construct
F
pulldown: resin H: Ni-NTA, S: Strep-Tactin
FSC
18Å
0.143
1/Å
90°
90°
G
BRE
MERIT40
RAP80
ABRAXAS
BRCC36
BRISC dimer negative stain EM map
BRCA1-A without RAP80 negative stain EM map, Kyrieleis et al., 2016
H
I
BRISC dimer negative stain EM map
BRCC36
BRE
BRISC models BRISC-SHMT2 cryo-EM
J
SIM-UIM
flexible linker
AIR
zinc finger
structure propensity calculation smoothened weighted score
RAP80
719

Figure S4. Functionalization of BRCA1-A by RAP80 and ABRAXAS, Related to Figures 2 and 3

(A) Alignment of RAP80 from human, mouse, pig, frog, and chimaera, shows highly conserved AIR domains. The label for the conserved tryptophan residue refers to the position in the human/mouse protein.

(B) Expression of GFP-fusion RAP80 constructs (star denotes unspecific band) was controlled by western blotting with an antibody against GFP.

(C) The minimal ABRAXAS binding region observed in the structure is essential for RAP80 binding to ubiquitin in vivo. Wild-type and RAP80 knockout U2OS cells were transfected with either GFP-NLS, GFP-RAP80 or GFP-RAP80ΔAIR. Cells were irradiated and focus formation was monitored by staining for MDC1 and BRCA1. The right panel shows the BRCA1 stained cells of the central panel with individual foci enlarged for comparison. BRCA1 foci were formed in wild-type cells as well as in KO cells transfected with wild-type RAP80. RAP80 devoid of the AIR domain forms RAP80 foci comparable to wild-type RAP80 but was unable to rescue BRCA1 focus formation, giving rise to fewer and smaller BRCA1 foci.

(D) Quantification shows a reduction of BRCA1 focus size by almost 50% in RAP80 KO cells that cannot be rescued by transfection with GFP-RAP80ΔAIR. Error bars represent mean ± SD. Number of replicates: WT n = 134, WT + RAP80 n = 56, WT + RAP80ΔAIR n = 45, RAP80 KO n = 107, RAP80 KO + RAP80 WT n = 50, RAP80 KO + RAP80ΔAIR n = 71.

(E) Co-expression of tagged subunits in insect cells was used to assess integration of RAP80 into BRCA1-A and BRISC. BRCA1-A integrates RAP80 stoichiometrically when co-expressed in insect cells, as shown for two independently generated sets of baculoviruses encoding BRCA1-A subunits. Co-expression of RAP80 with BRISC subunits on the other hand does not result in stoichiometric integration of RAP80 into the complex.

(F) The structure of BRISC was determined by 3D reconstruction from negative stain electron micrographs. Negative stain electron micrographs (scale bar: 150 Å), class averages, the FSC curve (18Å at FSC = 0.143) and a three-dimensional reconstruction are shown.

(G) Rigid body fitting of the BRCA1-A crystal structure into the BRISC dimer map (left) and the truncated RAP80-less BRCA1-A (Kyrieleis et al., 2016) map (right) shows that BRE and MERIT40 adopt a different conformation in fully assembled BRCA1-A with integrated RAP80 than in the two RAP80-less complexes.

(H) Negative stain electron micrograph (scale bar: 150 Å) and class averages of GraFix crosslinked BRCA1-A shows the single arc conformation only.

(I) Dimerization of BRISC is effected by an interaction between BRCC36 and BRE.

(J) Aside from the AIR domain embedded into BRCA1-A complex, RAP80 is largely flexible and unstructured as evidenced by structure prediction analysis of RAP80 sequence and by prevalence of monolinks in crosslinking-MS experiments of BRCA1-A complex.

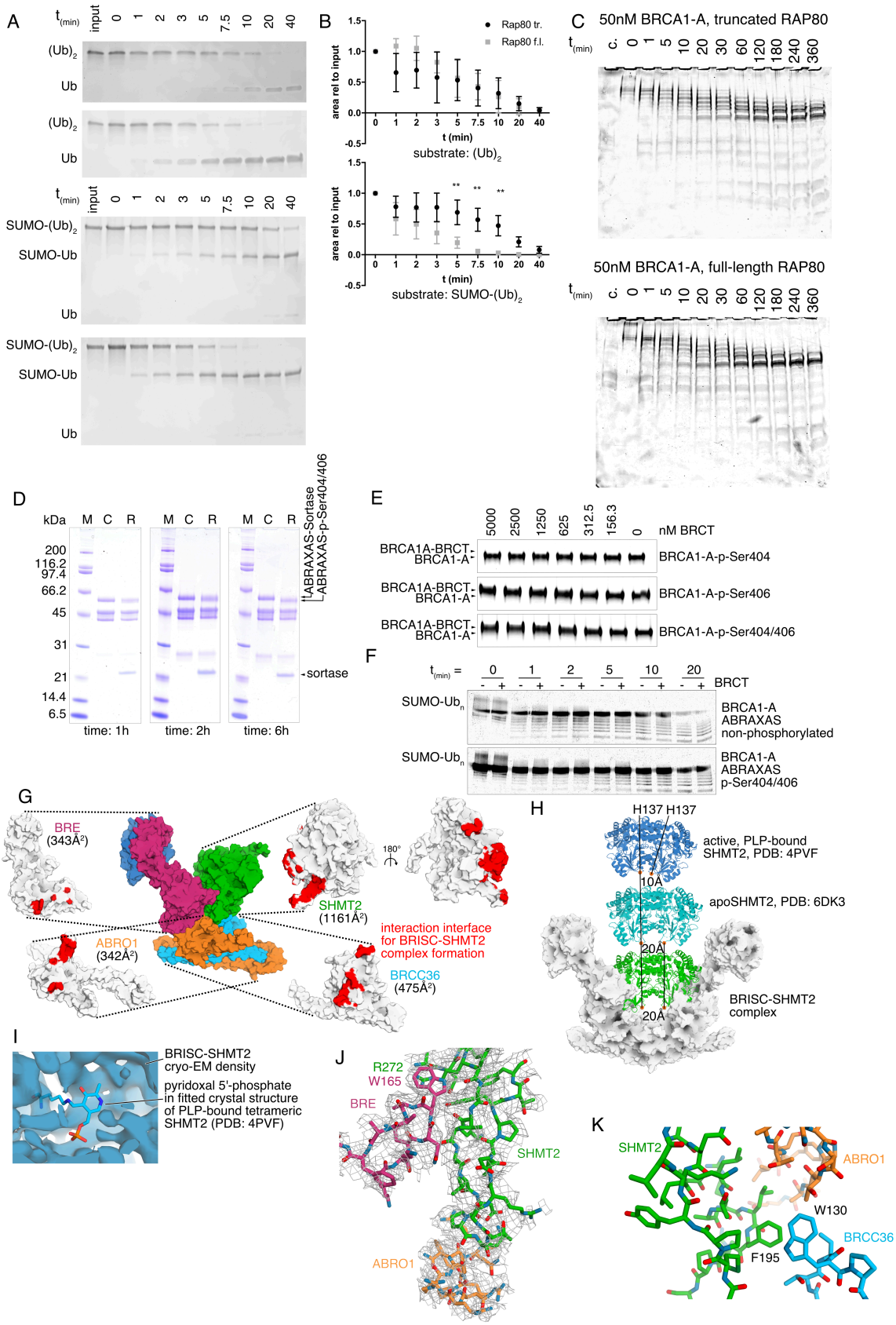
A
t(min) input 0 1 2 3 5 7.5 10 20 40
(Ub)2
Ub
SUMO-(Ub)2
SUMO-Ub
B
Rap80 tr.
Rap80 f.l.
area rel to input
t (min)
substrate: (Ub)2
substrate: SUMO-(Ub)2
C
50nM BRCA1-A, truncated RAP80
50nM BRCA1-A, full-length RAP80
t(min) c. 0 1 5 10 20 30 60 120 180 240 360
D
kDa M C R
200
116.2
97.4
66.2
45
31
21
14.4
6.5
ABRAXAS-Sortase
ABRAXAS-p-Ser404/406
sortase
time: 1h
time: 2h
time: 6h
E
5000 2500 1250 625 312.5 156.3 0 nM BRCT
BRCA1A-BRCT-BRCA1-A
BRCA1-A-p-Ser404
BRCA1-A-p-Ser406
BRCA1-A-p-Ser404/406
F
t(min) = 0 1 2 5 10 20
BRCT
SUMO-Ubn
BRCA1-A ABRAXAS non-phosphorylated
BRCA1-A ABRAXAS p-Ser404/406
G
BRE (343Å2)
ABRO1 (342Å2)
SHMT2 (1161Å2)
BRCC36 (475Å2)
180°
interaction interface for BRISC-SHMT2 complex formation
H
H137 H137
active, PLP-bound SHMT2, PDB: 4PVF
10Å
apoSHMT2, PDB: 6DK3
20Å
20Å
BRISC-SHMT2 complex
I
BRISC-SHMT2 cryo-EM density
pyridoxal 5'-phosphate in fitted crystal structure of PLP-bound tetrameric SHMT2 (PDB: 4PVF)
J
R272
W165
BRE
SHMT2
ABRO1
K
SHMT2
ABRO1
W130
BRCC36
F195

Figure S5. BRCA1-A DUB activity, BRCA1 sequestration and BRISC-SHMT2α interactions. Related to Figure 3, 4, and 5.

(A) Specificity of BRCA1-A in degrading Ubiquitin and mixed chains was assessed using BRCA1-A with full-length or truncated RAP80 and di-Ubiquitin or SUMO-di-Ubiquitin as substrates. Deubiquitination reactions were sampled, analyzed and quantified by SYPRO Ruby staining.

(B) BRCA1-A with full-length RAP80 degrades SUMO-di-Ubiquitin faster compared to BRCA1-A complex with truncated RAP80. Degradation speed of $(Ub)_2$ is independent of the presence of the RAP80 SIM-UIM_2 domains. Error bars represent mean ± SD of n = 3 replicates.

(C) Long K63-linked $(SUMO)_4$-$(Ub)_n$ chains are rapidly degraded by BRCA1-A irrespective of the presence or absence of the RAP80 SIM-UIM_2 domains.

(D) Progress of the sortase labeling reaction of engineered BRCA1-A with phosphorylated C-terminal ABRAXAS peptides is shown by band shift in SDS-PAGE.

(E) BRCA1-BRCT binds BRCA1-A when ABRAXAS is phosphorylated either p-Ser404 or p-Ser404/406, but does not form larger aggregates, as evidenced by shift on native PAGE.

(F) Binding of BRCA1-BRCT does not attenuate DUB activity against long mixed SUMO-Ubiquitin chains. Timed deubiquitination reactions were analyzed by SDS-PAGE and silver stain.

(G) SHMT2α binds to three subunits of BRISC: BRE, ABRO1 and BRCC36. Subunits are shown in white with the interaction surfaces shown in red.

(H) The SHMT2α dimer binds BRISC in a conformation similar to the inactive, apoSHMT2α, where the distance between His137 of the respective protomers is ~20 Å, instead of the conformation in the active, PLP-bound SHMT2α, where His137 of both protomers are more proximal at ~10 Å distance.

(I) PLP is absent in the BRISC-SHMT2α complex cryo-EM density.

(J) The SHMT2α BRISC-binding loop is extending towards BRE and ABRO1. Interactions between Arg272 of SHMT2α and Trp165 of BRE and between Arg153 and Tyr154 of ABRO1 and Asp279 and Pro280 of SHMT2α are observed.

(K) SHMT2α interacts with BRCC36: Phe195 of SHMT2α binds Trp130 of BRCC36.

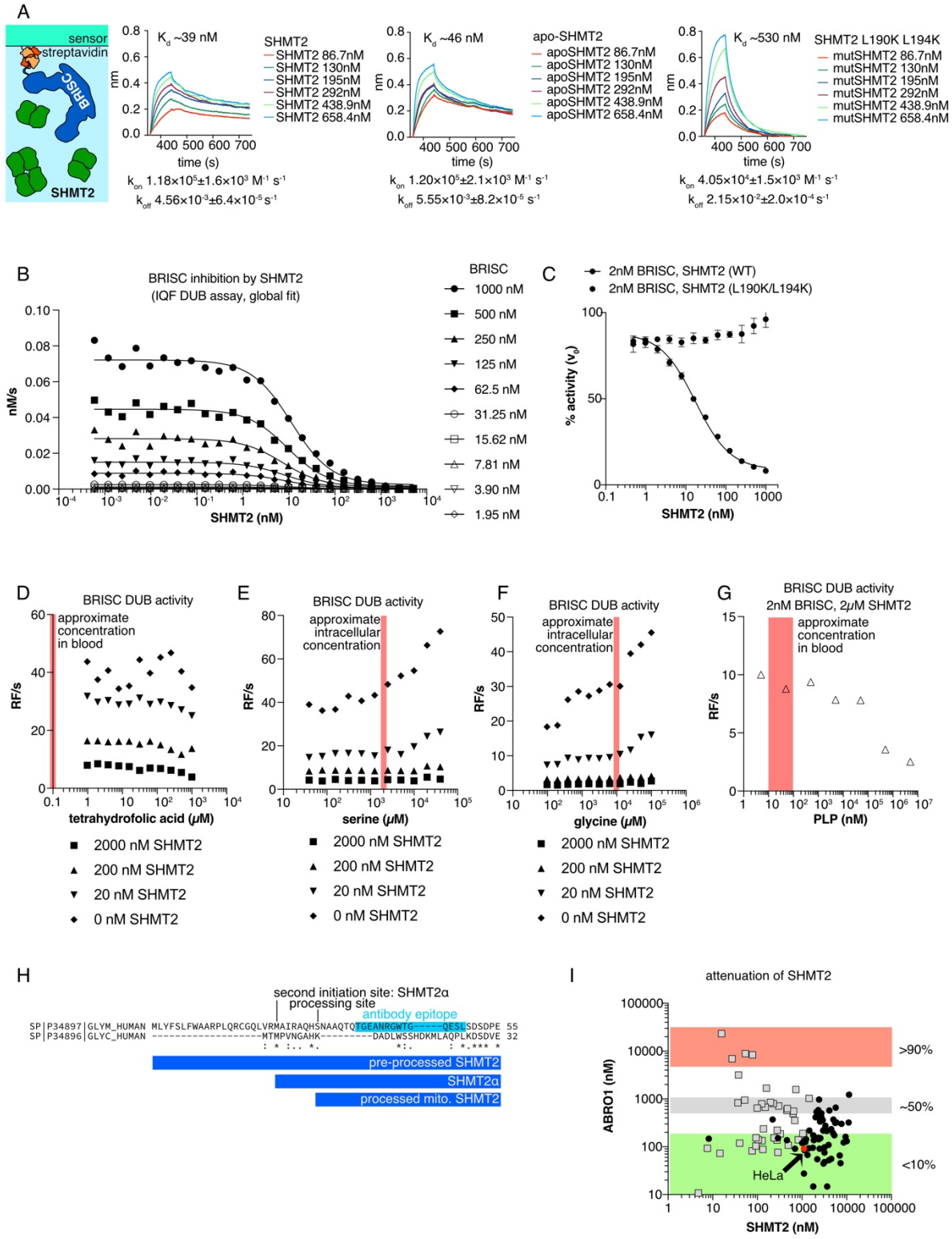
A
sensor
streptavidin
BRISC
SHMT2
K_d ~39 nM
SHMT2
SHMT2 86.7nM
SHMT2 130nM
SHMT2 195nM
SHMT2 292nM
SHMT2 438.9nM
SHMT2 658.4nM
nm
time (s)
k_on 1.18×10^5±1.6×10^3 M^-1 s^-1
k_off 4.56×10^-3±6.4×10^-5 s^-1
K_d ~46 nM
apo-SHMT2
apoSHMT2 86.7nM
apoSHMT2 130nM
apoSHMT2 195nM
apoSHMT2 292nM
apoSHMT2 438.9nM
apoSHMT2 658.4nM
k_on 1.20×10^5±2.1×10^3 M^-1 s^-1
k_off 5.55×10^-3±8.2×10^-5 s^-1
K_d ~530 nM
SHMT2 L190K L194K
mutSHMT2 86.7nM
mutSHMT2 130nM
mutSHMT2 195nM
mutSHMT2 292nM
mutSHMT2 438.9nM
mutSHMT2 658.4nM
k_on 4.05×10^4±1.5×10^3 M^-1 s^-1
k_off 2.15×10^-2±2.0×10^-4 s^-1
B
BRISC inhibition by SHMT2
(IQF DUB assay, global fit)
nM/s
SHMT2 (nM)
BRISC
1000 nM
500 nM
250 nM
125 nM
62.5 nM
31.25 nM
15.62 nM
7.81 nM
3.90 nM
1.95 nM
C
2nM BRISC, SHMT2 (WT)
2nM BRISC, SHMT2 (L190K/L194K)
% activity (v_0)
SHMT2 (nM)
D
BRISC DUB activity
approximate concentration in blood
RF/s
tetrahydrofolic acid (μM)
2000 nM SHMT2
200 nM SHMT2
20 nM SHMT2
0 nM SHMT2
E
BRISC DUB activity
approximate intracellular concentration
RF/s
serine (μM)
2000 nM SHMT2
200 nM SHMT2
20 nM SHMT2
0 nM SHMT2
F
BRISC DUB activity
approximate intracellular concentration
RF/s
glycine (μM)
2000 nM SHMT2
200 nM SHMT2
20 nM SHMT2
0 nM SHMT2
G
BRISC DUB activity
2nM BRISC, 2μM SHMT2
approximate concentration in blood
RF/s
PLP (nM)
H
second initiation site: SHMT2α
processing site
antibody epitope
SP|P34897|GLYM_HUMAN MLYFSLFWAARPLQRCGQLVRMAIRAQHSNAAQTQTGEANRGWTG-----QESLSDSDPE 55
SP|P34896|GLYC_HUMAN ----------MTMPVNGAHK---------DADLWSSHDKMLAQPLKDSDVE 32
pre-processed SHMT2
SHMT2α
processed mito. SHMT2
I
attenuation of SHMT2
ABRO1 (nM)
SHMT2 (nM)
>90%
~50%
<10%
HeLa

Figure S6. SHMT2α is an inhibitor of BRISC, related to Figures 5, 6 and 7

(A) SHMT2α binds BRISC with nanomolar affinity in a biolayer interferometry (BIF) experiment. Raw kinetic traces are shown, phase shift (nm) vs time (s); k_{on} and k_{off} were determined by global fit. SHMT2α lacking the PLP cofactor (apoSHMT2) binds with the same affinity as PLP-preincubated SHMT2α to BRISC in BIF. Raw kinetic traces are shown; k_{on} and k_{off} were determined by global fit. Mutation of Leu190 and Leu194 of SHMT2α to lysine increases k_{on} and k_{off}, reducing the affinity of SHMT2α for BRISC by an order of magnitude in BIF. Raw kinetic traces are shown; k_{on} and k_{off} were determined by global fit.

(B) SHMT2α inhibits BRISC with nanomolar K_i in an internally quenched fluorescent (IQF) di-ubiquitin assay. The reaction was set up in dilution replicates (n = 10) and K_i was determined by global fit.

(C) The Leu190Lys Leu194Lys SHMT2α mutant, which binds with far lower affinity than the wild type does not inhibit BRISC in the IQF DUB assay. Error bars represent mean ± SD of n = 3 replicates.

(D) Tetrahydrofolic acid does not affect activity of BRISC or inhibition by SHMT2α in the IQF DUB assay at concentrations around and above those found in human blood (Wishart et al., 2017).

(E) Serine does not affect activity of BRISC or inhibition by SHMT2α in the IQF DUB assay at concentrations around and above those found inside human cells (Chaneton et al., 2012).

(F) Glycine does not affect activity of BRISC or inhibition by SHMT2α in the IQF DUB assay at concentrations around and above those found inside human cells (Chaneton et al., 2012).

(G) Pyridoxal 5'-phosphate does not affect activity of BRISC or inhibition by SHMT2α in the IQF DUB assay at concentrations around and above those found in human blood (Wishart et al., 2017).

(H) Schematic representation of SHMT2 N-terminus processing. The SHMT2 gene gives rise to three isoforms of the enzyme: pre-processed SHMT2, SHMT2α and processed, mitochondrial SHMT2.

(I) Estimated concentrations of ABRO1 and SHMT2 for human tissues (gray rectangles) and cell lines (black circles). Estimated regions of low (green), medium (grey) and high attenuation (red) of SHMT2 function are shown. HeLa cells are shown in red. This figure assumes that inhibition kinetics of SHMT2 by BRISC is analogous to BRISC inhibition by SHMT2.

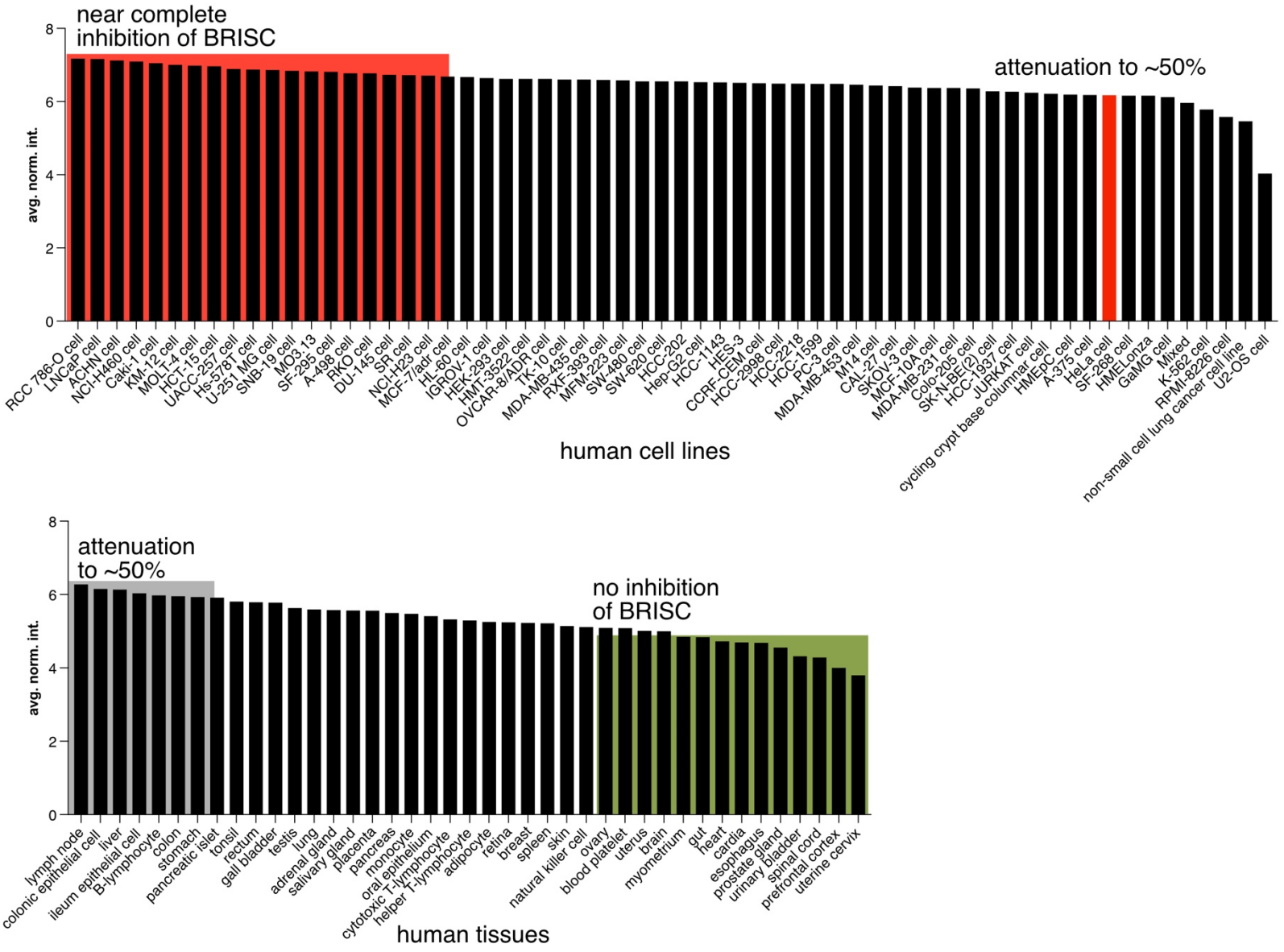
near complete
inhibition of BRISC
attenuation to ~50%
avg. norm. int.
0
2
4
6
8
RCC 786-O cell
LNCaP cell
ACHN cell
NCI-H460 cell
Caki-1 cell
KM-12 cell
MOLT-4 cell
HCT-15 cell
UACC-257 cell
Hs-578T cell
U-251 MG cell
SNB-19 cell
MO3.13
SF-295 cell
A-498 cell
RKO cell
DU-145 cell
SR cell
NCI-H23 cell
MCF-7/adr cell
HL-60 cell
IGROV-1 cell
HEK-293 cell
HMT-3522 cell
OVCAR-8/ADR cell
TK-10 cell
MDA-MB-435 cell
RXF-393 cell
MFM-223 cell
SW-480 cell
SW-620 cell
HCC-202
Hep-G2 cell
HCC-1143
HES-3
CCRF-CEM cell
HCC-2998 cell
HCC-2218
HCC-1599
PC-3 cell
MDA-MB-453 cell
M14 cell
CAL-27 cell
SKOV-3 cell
MCF-10A cell
MDA-MB-231 cell
Colo-205 cell
SK-N-BE(2) cell
HCC-1937 cell
JURKAT cell
cycling crypt base columnar cell
HMEpC cell
A-375 cell
HeLa cell
SF-268 cell
HMELonza
GaMG cell
Mixed
K-562 cell
RPMI-8226 cell
non-small cell lung cancer cell line
U2-OS cell
human cell lines
attenuation
to ~50%
no inhibition
of BRISC
avg. norm. int.
0
2
4
6
8
lymph node
colonic epithelial cell
liver
ileum epithelial cell
B-lymphocyte
colon
stomach
pancreatic islet
tonsil
rectum
gall bladder
testis
lung
adrenal gland
salivary gland
placenta
pancreas
monocyte
oral epithelium
cytotoxic T-lymphocyte
helper T-lymphocyte
adipocyte
retina
breast
spleen
skin
natural killer cell
ovary
blood platelet
uterus
brain
myometrium
gut
heart
cardia
esophagus
prostate gland
urinary bladder
spinal cord
prefrontal cortex
uterine cervix
human tissues

Figure S7. SHMT2 reaches inhibitory concentrations in cancer cells, Related to Figure 6 The average normalized intensity for SHMT2 in the quantitative mass-spectroscopic study of Wilhelm et al., 2014 is shown for human tissues and human cell lines. The absolute concentration of SHMT2 in HeLa cells determined by Hein et al., 2015 (red bar) was used to infer the approximate absolute concentrations of SHMT2 in the other tissues and cell lines. At SHMT2 concentrations around 1 μM and concentrations of BRISC around 50 nM, as found in HeLa cells, BRISC DUB activity is reduced by 50%. Most human tissues have lower concentrations of SHMT2, suggesting that BRISC action is attenuated in some tissues (gray), but not others (green). Cancer cell lines have far higher concentrations of SHMT2 than human tissues: most cancer cell lines surveyed contain higher concentrations of SHMT2 than HeLa, suggesting that BRISC DUB activity is nearly completely inhibited (red) in most cancer cell lines.